UNIVERSITAT POLITÈCNICA DE VALÈNCIA

ESCUELA TÉCNICA SUPERIOR INGENIEROS INDUSTRIALES VALENCIA

TRABAJO FIN DE MASTER EN INGENIERÍA QUÍMICA

STUDY OF THE PHOTOELECTROCATALYTIC PRODUCTION OF HYDROGEN FROM WATER USING GRAPHENE-BASED MATERIALS.

AUTHOR: JAVIER VAN HERPT VALDIVIA

SUPERVISOR: DR. SERGIO NAVALÓN OLTRA

SUPERVISOR: DR. JOSEP ALBERO SANCHO

Academic year: 2018-19

Resumen

El TFM está orientado a que el alumno adquiera destreza en la preparación, ensayo y caracterización de materiales grafénicos para su empleo como fotoelectrodo en la reacción de disociación de la molécula de agua para obtener hidrógeno. Se propone que el sustrato sea cuarzo, no conductor. Sobre dicho sustrato se preparará una lámina de múltiples capas de grafeno a partir de un precursor de origen renovable, ácido algínico, y se realizará un tratamiento de plasma de oxígeno. Se caracterizará mediante distintas técnicas y se relacionarán sus características con los resultados obtenidos en los ensayos en función de los defectos generados durante el tiempo de tratamiento. Después de realizar los ensayos, el alumno también realizará un análisis de costes de la investigación.

Palabras clave: Grafeno, hidrógeno, caracterización, fotoelectrocatálisis, defectos, material grafénico, voltametría cíclica, carga/descarga galvanostática

Resum

El TFM està orientat a que l'alumne adquirisca destresa en la preparació, assaig i caracterització de materials grafènics per al seu ús com fotoelectrode en la reacció de dissociació de la molècula d'aigua per a obtindre hidrogen. Es proposa que el substrat sigui quars, no conductor. Sobre aquest substrat es prepararà un film de múltiples capes de grafè a partir d'un precursor d'origen renovable, àcid algínic, i es realitzarà un tractament de plasma d'oxigen. Es caracteritzarà mitjançant diferents tècniques i es relacionaran les seves característiques amb els resultats obtinguts en els assajos en funció dels defectes generats durant el temps de tractament. Després de realitzar els assajos, l'alumne també realitzarà una anàlisi de costos de la investigació.

Paraules clau: Grafè, hidrogen, caracterització, fotoelectrocatàli, defectes, material grafènic, voltametria cíclica, carrega/descarrega galvanostàtica

Abstract

This master's dissertation goal is that the student to acquires skills in the preparation, testing and characterization of graphene materials for use as a photoelectrode in the water-splitting reaction in order to obtain hydrogen. It is proposed to use quartz as the substrate, not conductive. On said substrate a multilayer graphene film will be prepared from a precursor of renewable origin, alginic acid, and an oxygen plasma treatment will be carried out on it. It will be characterized by different techniques and its characteristics will be related to the results obtained in the tests according to the defects generated during the treatment time. After conducting the essays, the student will also perform a cost analysis of the research.

Key words: Graphene, hydrogen, characterization, photoelectrocatalysis, defects, graphenic material, cyclic voltammetry, galvanostatic charge/discharge

Contents

Part I

Memoir

Chapter 1

Introduction

1.1 Energy consumption growth: The environmental need

The amount of energy needed by society has grown since the Industrial Revolution as well as the amount of Greenhouse Gases (GHG) released to the atmosphere. One of the reasons of this increase in the amount of GHG is that the main power source has been the fossil fuels and nowadays society keeps relying on it. In the last half century the amount of energy consumption has been almost quadrupled, from a yearly average of 16 PW·h up to 58 PW·h as can be seen in figure 1.1.

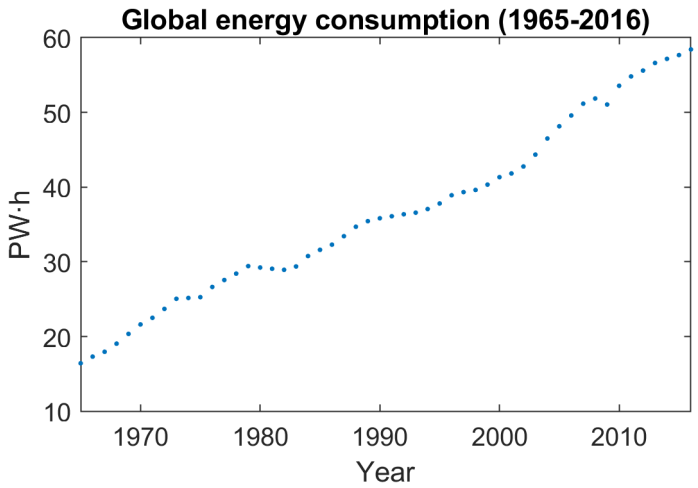

Figure 1.1: Global energy consumption from 1965 to 2016. Data from British Petroleum[1]

The indiscriminate burn of fossil fuels has environmental consequences that are altering the climatic conditions in the globe and the air, water and soil composition. The environmental and/or health problematic of the burn of fossil fuels include:

- **Air pollution:** The combustion of fossil fuels results in the emission of pollutants which can be harmful for the environment as well as the public health. These pollutants may depend on the nature of the fossil fuel and can be:
  - *Particles:* Burning fossil fuels generates soot that can cause health problems related to breathing.
  - *Nitrogen oxides (NOx):* These are produced during the combustion of fossil fuels in air. Air is mainly composed of nitrogen and oxygen. Due to the high temperatures of combustion nitrogen reacts with oxygen in order to generate nitrogen oxides. These oxides contribute to the formation of acid rain and tropospheric ozone, which may derive into respiratory diseases.
  - *Sulphur dioxide (SO_2):* It's mainly produced by the combustion of coal and contributes to acid rain, particle formation and can derive into respiratory diseases.
- **Greenhouse gases emissions:** The combustion of fossil fuels produces large amounts of greenhouse gases. The main emission is carbon dioxide, CO_2, but other GHG like methane, CH_4, can be emitted due to an incomplete combustion. In the last 650.000 years there have been seven cycles of glacial advance and retreat and the amount of atmospheric CO_2 has been oscillating between 180 and 300 ppm, amount which never had been exceeded. Most of these climate changes are attributed to small orbit variations of Earth. The burn of fossil fuels increased the amount of atmospheric carbon dioxide from 310 ppm in the 1950s up to around 400 ppm, figure 1.2, nowadays.[2]

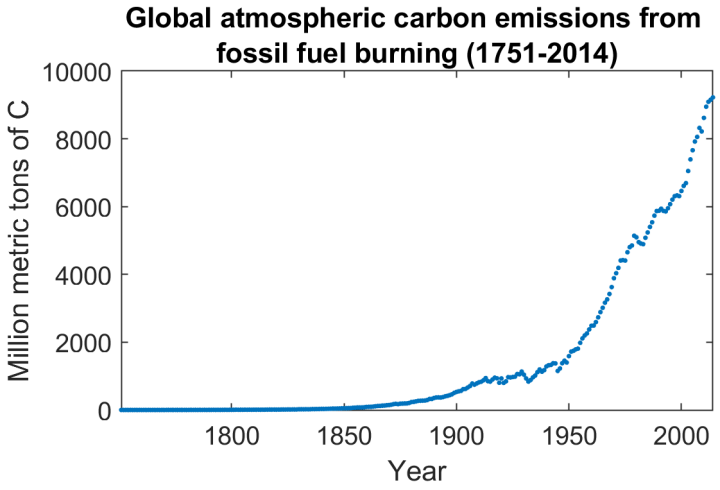

Figure 1.2: Global atmospheric carbon emissions. Can be approximated to CO_2 emissions multiplying by 3.67 the amount of C. Data from U.S. Department of Energy[3]

- **Toxic waste:** The set-up of the crude produces toxic waste as well as the ashes of coal are rich on heavy metals, which vary depending on the origin of the fossil fuel.
- **Oil spills and gas releases:** During the extraction, transport or transformation of the oil may occur a spill. These spills can contaminate both water and soil. Lighter fractions

of crude such as CH_4 can be released to the atmosphere during perforations or because of leaks.

Despite the environmental and public health issues that arise from the use and exploitation of fossil fuels, it must be taken into account that it is also a limited, non-renewable resource, which sooner or later will be depleted or its exploitation will be so costly that it will not be viable to use it as an power source.

1.2 Renewable and clean energy as an answer

There are several renewable alternatives which can provide clean energy:

- Wind power
- Hydropower
- Marine power
- Geothermal power
- Biomass power
- Solar power

Of all these energy sources, solar power is very attractive because it's unlimited and it could be a total alternative to fossil fuels because the sun irradiates earth's surface at an average rate of 120000 TW, which is about 4 orders of magnitude larger than the worldwide average technological energy use [4] (Below 10 TW).

The main drawbacks of this energy source are its circadian nature and that it depends a lot on the weather conditions, so its energy can only be harvested during a window of time during the day and the amount is limited by climatological phenomena and the season of the year.

Solar power is mostly harnessed through:

- **Solar accumulators:** Solar power is transformed into heat.
- **Photovoltaic panels:** Solar power its transformed into electrical power through the photovoltaic effect.
- **Photocatalysis:** Solar powered is used to accelerate or make possible a chemical reaction. The energy can be chemically stored in form of bonds.

Both the solar accumulators and photovoltaic panels can be used to obtain electrical power. The problem is that they can only generate electricity during sunny hours and if the weather conditions are favorable. The peaks of production should also coincide with those of energy demand, which will not be usual.

Photocatalysis can be a way harvest the solar energy and store it into chemical bonds making possible the release of energy when necessary. In other words, it can be a way of producing **solar fuels**.

1.3 Solar fuels

Solar fuels are chemical compounds produced by solar energy and can be used when its energy is needed, whether there's sunlight or not. Some of the solar fuels produced by photocatalysis are:

- **Hydrogen (H_2):** Produced by water splitting.
- **Methane (CH_4):** Produced by carbon dioxide reduction.
- **Methanol (H_3COH:** Produced by carbon dioxide reduction.
- **Methanoic acid (HCOOH):** Produced by carbon dioxide reduction.

1.3.1 Hydrogen - H_2

Hydrogen is one of the most abundant elements on the earth's surface although its presence in molecular form is in traces it can be found in chemical compounds such as hydrocarbons and water. It's produced naturally by anaerobic bacteria and algae but its mass is so low that it can escape the gravitational pull of the earth causing that even being produced by microorganisms its concentration in the atmosphere is bellow 1 ppm. As can be seen in table 1.1 hydrogen has got a high specific energy.

Table 1.1: Heating values of comparative fuels. Data from Hydrogen Fuel Cell Engines[5].

Fuel	Higher Heating Value (at 25 °C and 1 atm)	Lower Heating Value (at 25 °C and 1 atm)
Hydrogen	141.86 kJ/g	119.93 kJ/g
Methane	55.53 kJ/g	50.02 kJ/g
Propane	50.36 kJ/g	45.6 kJ/g
Gasoline	47.5 kJ/g	44.5 kJ/g
Diesel	44.8 kJ/g	42.5 kJ/g
Methanol	19.96 kJ/g	18.05 kJ/g

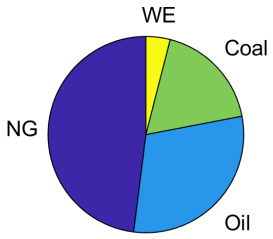

Figure 1.3: Global hydrogen production feedstocks. NG: natural gas (48 %), oil (30 %), coal (18 %), WE: water electrolysis (4 %).

Hydrogen can be produced through different ways. It can obtained from fossil fuels, a non-renewable and polluting feedstock; from biomass or from water splitting. Nowadays, the main feedstocks for hydrogen production are natural gas, oil, coal and water electrolysis[6, 7], figure 1.3. As can be observed, 96 % of the feedstocks used to produce hydrogen are fossil fuels, resulting in close to 500 Mt of CO_2 to the atmosphere [8]. According to the 2DS-High H_2 scenario published in the Energy Technology Perspectives 2012 of the International Energy Agency[9], 15 % of the fuel demand for vehicles will be accounted by hydrogen. Hydrogen will also be accountable of a significant part of the industrial and building energy. As the hydrogen requirements grow, so will grow the hydrogen production and its related CO_2 emissions, resulting in an even less sustainable scenario because of the non-renewable nature of fossil fuels and its emissions. To avoid that, CO_2 capture will be needed as well as increasing the portion that water electrolysis occupies in the figure 1.3.

1.3.2 Water Splitting

Water is a chemical substance formed by 2 atoms of hydrogen and an atom of oxygen. Its most common state is liquid and is one of the most abundant, it covers 71% of earth surface, and inexhaustible materials in Earth. Through water splitting[10] is possible to produce H_2 which after its use, if used as a solar fuel, will become water again.

The main advantages of water splitting processes are:

- They don't emit pollution when they're used with renewable energy sources
- The feedstock is abuntandant
- Oxygen is the only byproduct
- Contributes as an electricity storage option for the renewable energy sources.

Water splitting can be achieved by three different ways:

- **Thermolysis:** There are three main ways of decomposing water through this technique. Single stage water splitting requires a temperature higher than 2500 °C which makes it impracticable to perform through solar power. The other ways consist of a cycle of chemical reactions, multi-stage and two stage, but both of them require high temperatures: up to 500 °C for multi-stage and up to 1600 °C for the two step cycle.
- **Electrolysis:** Consists of providing the required energy by electricity (1.23 eV ideally). Must be taken into account that the water splitting reaction is very endothermic, making it a effective technique for water splitting but with a high energy cost.
- **Photocatalysis:** Consists of using one or some photocatalysts capable of absorbing in the visible spectrum of light whose bandgap is above 1.23 eV and is aligned correctly to decompose the water into H_2 and O_2.

1.3.3 Electrolytic water splitting

Electrolysis was first discovered by Antoine Carlisle and William Nicholson back in the 1800 when they were learning about Alessandro Volta's voltaic pile. During their learning the generated bubbles of H_2 and O_2, they had discovered electrolysis of water. Nowadays it is the most effective technique for water splitting, although performed with the use of distinc electrolytes, electrodes and in some cases membranes. The most simple water electrolysis cell consists of two electrodes submerged in an electrolyte, figure 1.4. When electrical current is applied hydrogen may be generated at the cathode, equations 1.2 and 1.3, and oxygen at the anode, equations 1.4 and 1.5, if the potential is above 1.23 V vs NHE.

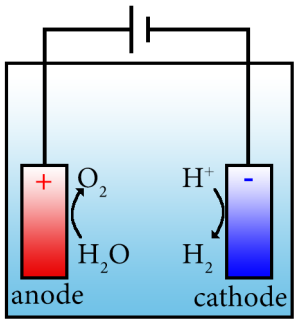

Figure 1.4: Simple water electrolysis cell.

The overall reaction of water splitting is:

$$2H_2O(l) \rightarrow O_2(g) + 2H_2(g) \tag{1.1}$$

The reaction that takes place in the cathode:
In acidic media:

$$2H^+(aq) + 2e^- \rightarrow H_2(g) \tag{1.2}$$

In basic media:

$$2H_2O(l) + 2e^- \rightarrow H_2(g) + 2OH^-(aq) \tag{1.3}$$

The reaction that takes place in the anode:
In acidic media:

$$2H_2O(l) \rightarrow O_2(g) + 4H^+ + 4e^- \tag{1.4}$$

In basic media:

$$2OH^-(aq) \rightarrow 1/2O_2(g) + H_2O + 2e^- \tag{1.5}$$

The main advantage of this method is that if the source of energy used to supply the 1.23 eV needed to split the molecule of water is a renewable source, the amount of GHG emitted to the atmosphere is zero.

The main disadvantage of this method is that the electrode materials used to efficiently produce hydrogen usually contain noble metals which have little abundance, are very expensive due to its abundance and some of them are unstable in the conditions they're used.

1.3.4 Photocatalytic water splitting

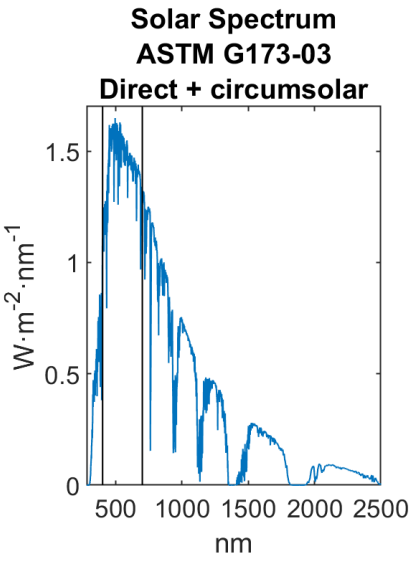

Figure 1.5: Solar spectrum (cut at 2500 nm) at sea level according to ASTM G173-03. Range of visible light between the black lines.

Since Fujishima and Honda performed the first photocatalytic water splitting back in 1972 using a rutile TiO_2 photoanode[11], photocatalytic water splitting through the use of semiconductors has been a field of research very studied and more than 100 of photocatalytic sustems based on metal oxides have been reported to produce hydrogen and oxygen on stoichometric ratio, 2:1. The main drawback of most of these semiconductors is that its bandgap is so wide that they work under ultraviolet radiation with a wavelength below 400 nm and visible wavelength is above this value, $400<\lambda<800$nm, where the sun radiates with greater intensity, figure 1.5, even if all the light energy in the UV region up to 400nm was harnessed and turned into H_2 witha 100% quantum energy, the maximum solar light conversion efficiency would be only 2%[12].

Photocatalytic water splitting, figure 1.6, under visible light using through semiconductor particles consists of the semiconductor material absorbing a photon whith an energy greater or equal to its band gap. This photon is capable of exciting an electron, e^-, that moves from the valence band (VB) to its conduction band (CB). When this happens holes, h^+, are left in the valence band, equation 1.6. The excited status of the semiconductor is an unstable status and the electrons and the holes may perform the desired, or undesired, oxidation (equation 1.8) and reduction (equation 1.7) reactions or recombine

(equation 1.9) emitting light or generating heat. In order to make possible the water splitting reaction, the lowest unoccupied molecular orbital (LUMO) and the highest occupied molecular orbit (HOMO) must be arranged in such a way that the potential of the LUMO is bellow 0 V vs Normal hydrogen electrode (NHE) and the HOMO is above 1.23 V vs NHE.

$$\text{Semiconductor} \xrightarrow{h\nu} e^- + h^+ \tag{1.6}$$

$$2e^- + 2H^+ \rightarrow H_2 \tag{1.7}$$

$$4h^+ + 2H_2O \rightarrow O_2 + 4H^+ \tag{1.8}$$

$$e^- + h^+ \rightarrow \text{light or heat} \tag{1.9}$$

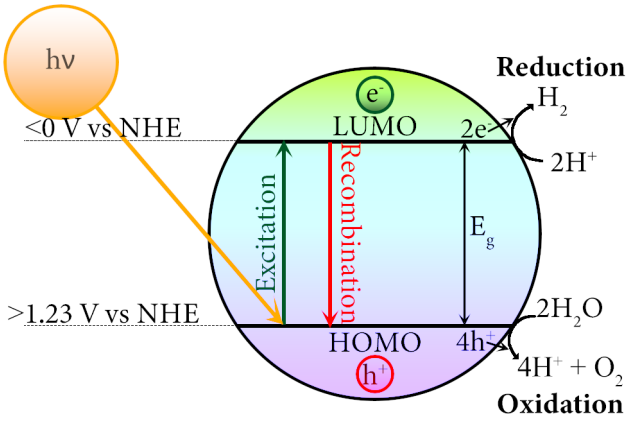

Figure 1.6: Simple schematic of photocatalytic water splitting over a semiconductor.

The main advantage of photocatalytic water splitting is that only with sunlight it's possible to excite a semiconductor and prouce hydrogen.

The main disadvantages are that most semiconductors with enough bandgap energy absorb in the ultraviolet, recombination of electrons and holes is high and most semiconductors that absorb in the visible spectrum don't have an adequate alignment of its HOMO and LUMO levels in order to carry out oxidation and reduction at the same time and sacrificial agents are needed.

1.3.5 Photoelectrocatalytic water splitting

Photoelectrolcatalytic water splitting[13] emerges as an option to take advantage of both techniques. Using a photocatalyst in conjuction of an electric circuit that supplies a potential differential that helps to decrease the amount of electron and hole recombination as well as a boost in the potential or increased current flow accelerating or making possible the reaction without using any sacrificial agent. The figure 1.7 represents a simple photoelectrocatallytic cell. It's very similar to a electrocatalytic cell, figure 1.4, but includes a source of light, figure 1.7.

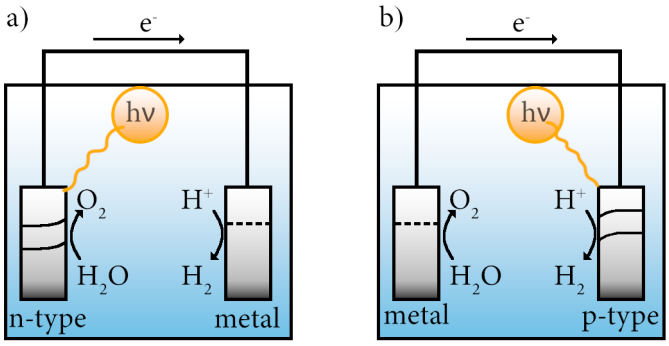

Figure 1.7: Different cell configurations for a photoelectrocatalytic water splitting cell. a) A cell featuring an n-type working electrode, which catalyzes the OER. b) A cell featuring an p-type working electrode, which is catalyzes the HER.

In these cells a photoelectrode is excited by light forming a electron-hole pair. If this photoelectrode is based on a n-type semiconductor and working as an anode, the potential applied forces the excited electron, that moved into the CB, to get separated and transfered to the cathode where it reduces water into H_2 while the holes gets transfered to the surface of the semiconductor and oxides water into O_2. In the case of p-type-semiconductor based photoelectrodes its surface is used to reduce water and water gets oxidized on the surface of the other electrode. If instead of using a p-type semiconductor photoelectrode or a n-type photoelectrode semiconductor both are used, it's possible achieve a photoelectrochemical system capable of reducing and oxidizing water into H_2 and O_2 respectively.[14]

1.4 Graphene

Graphene[15, 16], G, is an atom width structure, the thinnest known material, composed by sp^2 hybridized carbons disposed in an hexagonal array. Its thermal and current conductivities are remarkable, it is almost transparent and it is impermeable to gases. When enough planar sheets of G are perfectly stacked together graphite is formed whereas G can be obtained from graphite. When the G is doped with other 2D materials or heteroatoms it must be refered as a G-mat and some of its carbon atoms have been replaced by other elements.[17]

G-mats present catalytic activity, depending on the doping can behave as a n-type semiconductor or a p-type semiconductor, in addition to qualities such as thermal and electrical conductivity.

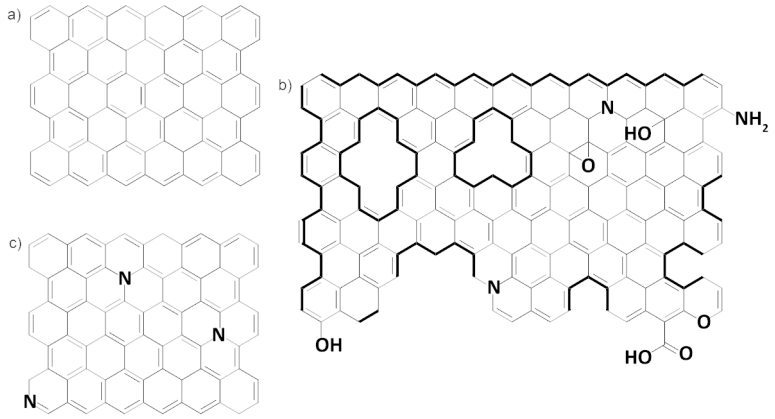

Figure 1.8: a) Graphene, b) Different active sites in deffective graphene, c) Nitrogen doped graphene.

G-mats are mainly prepared through:

- **Chemical oxidation - Hummers method:** The raw material used in this method is graphite and it's a two-step based oxidation. In first instance, graphite oxidation is started by potassium permanganate in a mixture of concentrated sulphuric and nitric acids. Then is added hydrogen peroxide that helps to oxidize the graphite. After the oxidation, the graphite oxide is exfolliated through sonication and GO is obtained. If the desired product is rGO then a thermal or chemical reduction takes place. This method is capable of large scale production of a medium quality graphene. Its downsides are the impurities and defects of the graphene, its low electrical conductivity and that during the process a large amount of liquid wastes are produced.[18]
- **Chemical vapor deposition:** Through this method is possible to obtain high quality graphene with absence of impurites at the cost of low production. This method consists on flowing a methane gas stream over hot metallic surfaces such as nickel or copper. The methane is dehydrogenated over the metal surface and carbon are sorted around the metal spheres. Then the metal sheet can be dissolved in an acid such as hydrochloric acid that does not damage the G.[19]
- **Mechanical exfoliation:** Mechanical exfoliation is how graphene was first produced. It consists in exfoliating graphite through the use of Scotch tape. The G obtained is of high quality but is a time consuming technique that yields a very low production.
- **Pyrolysis of suitable precursors:** This method can be used for large scale production, its associated costs are low, doping is easy and can be used with renewable resources such as biopolymers. Although the G obtained is of medium quality when its electrical properties are considered, the defects present in its structure improves catalytic reactions. It consists on the pyrolysis of a graphene precursor in a inhert atmosphere.

1.4.1 Defective graphene

Such as the ones that Lavorato et al.[20] and Garcia et al.[21, 22] reported: N-doped graphene films photoelectrodes for H_2 evolution could be produced from chitosan, figure 1.9, and Latorre-Sanchez[23] reported that P-doped graphene with the same purpose could be obtained from alginate, figure 1.10.

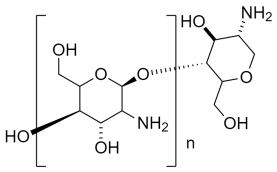

Figure 1.9: Chitosan molecular structure

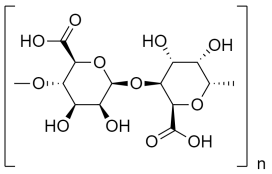

Figure 1.10: Alginate molecular structure

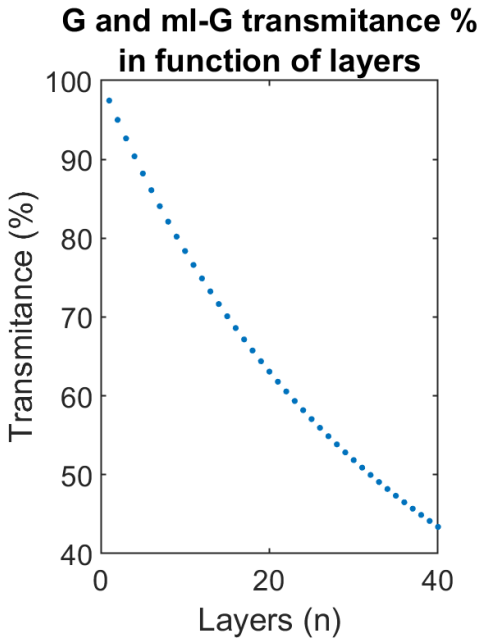

Figure 1.11: G and ml-G transmitance obtained from the Zhu's equation.

There different defects in graphene[24] can have different sources, amongst them:

- **Stone-Wales defects:** These defects are caused by the rotation of a pair carbon atoms in the hexagonal structure, causing that the adjacent rings transform into two pentagonal and two heptagonal rings.
- **Vacant defects:** When an atom or multiple atoms of carbon are missing from a hexagon ring, the material undergoes an Jahn-Teller distortion where some of the dangling bonds are connected together towards the missing atom in order to minimize energy.
- **Out-of-plane carbon adatoms:** A missing carbon atom may form new bonds on the surface of the graphene and form a 3D structure.
- **Heteroatoms:** A carbon in the hexagonal ring is replaced by other atom.

Defective graphene has been shown to have photocatalytic activity in [25], so from the point of view of catalysis must be taken into account that defects in the graphene can behave as active centers, so obtaining a partially oxidized graphene can be favorable. Keeping this on mind and that pyrolosys of precursors (biopolymers) does not produce toxic waste, this method could be best alternative to produce G-mat based catalysts which have a modulated band gap that changes the behaviour of graphene from being a conductor to a semiconductor.

Another factor to consider is that the transmitance of multilayer graphene, ml-G. Graphene is a layer of carbon atoms arranged in a hexagonal structure, sometimes refered as a honeycomb structure. When multiple layers of graphene are stacked the material is known as ml-G and its

transmittance lowers following a nonlinear negative exponential equation [26][27], absorbing more visible light in function of the layers of G or G-mat that are stacked. This factor must be taken into account when producing photocatalysts or photoelectrodes based on G, ml-G or G-mat which are meant to work under visible light conditions.

Chapter 2

Aim of this work

As the fossil fuel reliance depicts a global climate change that leads to many environmental as well as economic disasters because, and not only, of its exploitation and shortage, a way to eventually stop relying on it is needed. Graphene is a rather new material in its usage as sustainable and environmentally friendly catalyst that can be used in multiple industry processes, which amongst them is the water splitting reaction. Therefore, the aim of this work is to synthesize and characterize a graphene material capable of performing the water splitting reaction under photoelectrocatalytic conditions. Specifically, the aim of this Master's Dissertation is divided in the next goals:

- Synthesis of ml-G films through a top-bottom technique: Pyrolysis of a natural occurring polysaccharide, alginic acid, precursor.
- Introduction of defects in the ml-G films structrure through oxygen plasma treatment.
- Characterization of the G-mat films through:
  - Atomic force microscopy (AFM).
  - Raman spectroscopy.
  - Surface resistivity.
  - Ultraviolet-visible spectroscopy (UV-spectroscopy).
  - X-ray photoelectron spectroscopy (XPS).
- Testing of the photoelectrodes in an electrochemical cell.
- Quantification of the hydrogen production and identification of the best treatment.
- Validation of results.

Chapter 3

Experimental methodology

This chapter details the followed methodology in order to meet the goals as well as a brief explanation of the different characterization techniques and photoelectrocatalytic assays

3.1 Synthesis of G-mat films

3.1.1 Substrate preparation

Figure 3.1: Branson ultrasonic cleaner used with a container floating.

The synthesis of ml-G is performed over a quartz substrate, therefore the quartz must be prepared before. Quartz feedstock (2 cm x 2 cm) requires to be cleaned before the precursor can be coated.

In order to clean the quartz, the feedstock is placed inside a container in an ultrasonic cleaner, figure 3.1, with different solvents:

- Ethanol during 15 minutes.
- Acetone during 15 minutes.
- 18.2 MΩ water during 15 minutes.

After the three baths, the quartz is dried with the use of an air gun and stored in 1 M HCl solution.

3.1.2 Precursor preparation

The precursor used for the preparation of the ml-G films is alginic acid, but it is not used in powder. In order to make a film, a precursor solution must be prepared. The solution is composed of 800 mg alginic acid, 10 mL ultra-pure water (18.2 MΩ) and 1 mL of 25% ammonia solution. First the alginic acid powder is put inside a pot in a magnetic stirrer stirrer. Then the ammonia solution is added to the water and then its poured over the alginic acid and left stirring at 800 rpm until all the alginic acid is dissolved. After all the alginic acid is kept stirring for 2 hours at 100 rpm to let all the air bubbles leave the dissolution. At last the solution is filtered with the use of, multiple, 45 μM regenerated cellulose syringe filters.

3.1.3 Coating of the quartz with the precursor

In order to prepare ml-G films, first a thin film of precursor must be coated on the surface of the substrate. The technique used to prepare the precursor film is Spin-Coating[28] which is capable of making an uniform coat of a Newtonian fluid through radial drainage. To perform this part of the graphene film preparation, the previously cleaned quartz feedstock is fixed on top of the chuck, the part of the spin coater, figure 3.2 that spins, with double sided tape. Then, 1 mL of precursor solution is placed on top of the quartz and the spin coater is set to spin with the next parameters:

- Acceleration: 1000 rpm s^{-1}.
- Speed: 4000 rpm.
- Duration: 30 s.

After the spin coating, the quartz is removed with a pair of tweezers and left to dry on top of a hotplate set at 60 °C for 2 hours.

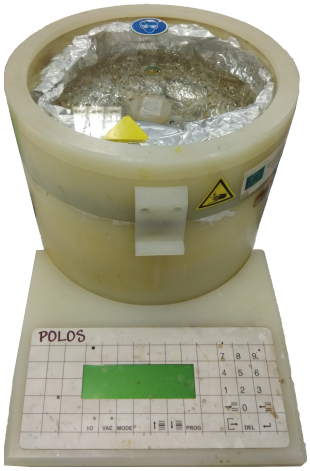

Figure 3.2: POLOS spin-coater used.

3.1.4 Pyrolysis of the precursor films

The last step on the preparation of ml-G films is to pyrolyze[29]. This step is carried on in a tube furnace under inhert atmosphere, Argon.

Figure 3.3: Side image explaining the disposition of coated quartz (red), quartz (blue) and tape (yellow) in the crucible (black).

First of all, the coated substrates are placed facing up in a crucible, figure 3.3, putting quartz separators bellow and on top of each piece of coated quartz. A total os 6 pieces of coated quartz are placed in the crucible separated with bigger pieces of raw quartz. A bigger piece of quartz is placed on top of the crucible for protecting the films from contamination during the pyrolysis.

This bigger piece of quartz is fixed to the sides of the crucible with two small pieces of Scotch tape for convenience to avoid the top piece of quartz from falling.

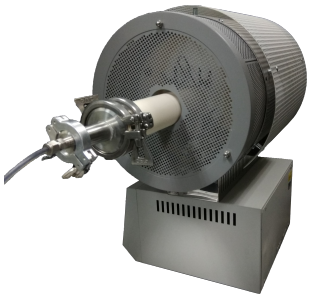

Figure 3.4: Tube furnace used.

Then the crucible is placed inside of a tube furnace, figure 3.4, and the furnace is set to work according to the next parameters:

- Argon flow rate: 200 mL min^{-1}.
- Set point temperature: 900 °C.
- Heating rate: 10 °C min^{-1}.
- Set time temperature hold: 2 h.

After the temperature hold, the furnace resistance shuts down and is left to cool. When the furnace reaches room temperature, the ml-G films over quartz substrates, figure 3.5, can be removed from the crucible and stored in a proper container for its future usage.

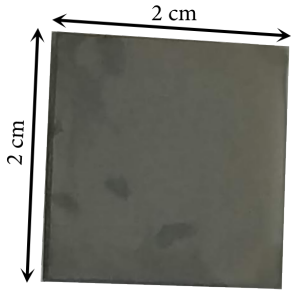

Figure 3.5: Example of a resulting ml-G film on a quartz substrate the dark spots are caused due to adhesive residue in the backside of the quartz.

3.1.5 Oxygen plasma treatment of ml-G

After the multilayer graphene films are prepared, the films are cut in two pieces of aproximately 2 cm x 1 cm. For this dissertation, the 2 cm x 2 cm ml-G films are marked with a diamond tip pencil on the clean side of the substrate. Then, the quartz and ml-G are split in two pieces using a Silberschnitt branded cut running plier.

Figure 3.6: Diener Femto plasma cleaner used to treat the ml-G films.

Once the films are split, two pieces of the same ml-G film are identified with a small mark in a corner of the clean side of the quartz and placed in a crucible and then inside the plasma cleaner. Then chamber is put under vacuum conditions for 20 minutes. After the vacuum, the oxygen gas valve is partially opened to set the chamber to 0.40 mbar and is left for 5 minutes to stabilize. Once the chamber has stabilized, the plasma generator is set to work at 10% power for different amounts of time depending on the sample 6 s, 12 s and 18 s, and then is powered on. Once the plasma treatment has finished, the oxygen valve is closed and the chamber is ventilated. After the chamber has reached atmospheric pressure, the samples are removed and stored. One half for later characterization and the photoelectrochemical testing.

3.1.6 Photoelectrode preparation

In order to prepare the photoelectrode, a rectangular area is delimited with polymeric insulating paint in the half G-mat on quartz stored for testing. Then, the polymeric paint is left to cure on a hot plate set at 60 °C during 2 hours. After curing, a 1 wt. % paraloid B-72 in acetone solution is prepared, paraloid B-72 is used to give mechanical stability to the G-mat, 50 μL cm^{-2} of paraloid solution is added to the delimited rectangular area of the electrode using a micropipette. Silver conductive paint is added to the top part of the G-mat in order to allow a better connection with the instruments and have a better current distribution over the photoelectrode. The resulting electrode, figure 3.7, is ready to be tested in the electrochemical reactor.

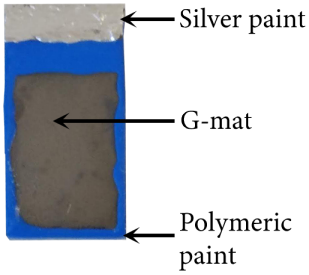

Figure 3.7: Example of a prepared photoelectrode.

3.2 Characterization

This section is dedicated to explaining the different characterization techniques used.

3.2.1 Atomic force microscopy

Figure 3.8: Buker Multimode8-HR atomic force microscope used.

Atomic force microscopy[30], figure 3.8, is a scanning probe microscopy technique. It consists of a tapping probe, a conducting metal tip, that is held close to the sample, between 0.3 nm and 1 nm above. As the tip surveys the sample it oscillates due to interactions with the surface and is measured with a laser. Then, it is translated as z axis variation. Together with the translation of the x and y axis a 3D image with a high resolution, up to a subnanometer scale, can be obtained. This technique is used to have a visual variation of the photoelectrode material in function of the plasma treatment time as well as parameters such as surface rugosity and material thickness. In order to be able to measure the film thickness, a scratch made in the film exposing the substrate had to be made. According to the standard ISO-25178, the surface rugosity is the root mean square height of the surface (Sq). The Kurtosis of height distribution is also obtained following the same standard.

3.2.2 Raman spectroscopy

Raman spectroscopy[31], figure 3.9, is a high resolution technique capable of analyzing compounds, whether organic or not, by using a monochromatic light beam that is capable of exciting the molecules to a higher energy state. These high energy states are quickly vacated and the energy is released in the form of scattered photons of a determinated wavenumber which is compared with the excitation light wavenumber. The difference between them is known as the Raman shift.

Figure 3.9: Renishaw branded Raman spectrophotometer used.

When graphene materials are analyzed, figure 3.10, three peaks appear in the Raman shift. These peaks are known as D peak, at 1350 cm^{-1}; G peak, at 1580 cm^{-1}; and 2D band, around 2700 cm^{-1}. D band shows how disordered is the material, G band reefers to the graphitic carbon and the 2D band reefers to the stacking of the graphene layers[30].

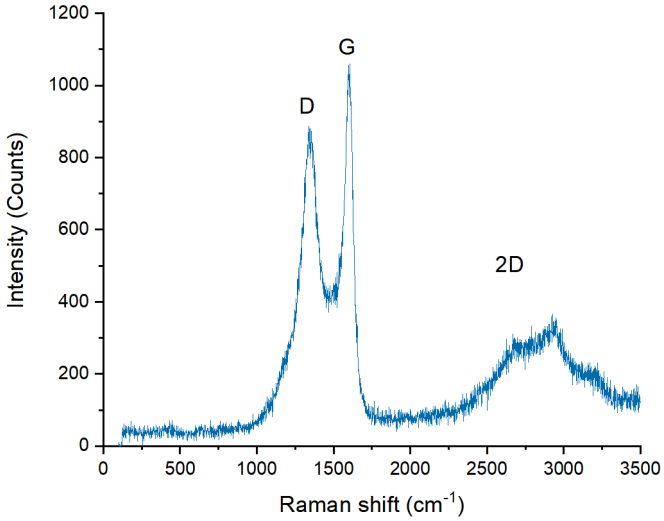

Figure 3.10: Example of a G-mat Raman spectroscopy with the D and G peaks and 2D band identified.

3.2.3 Surface resistivity

Surface resistivity is the resistance between the two opposite edges of a 1 cm^2 surface film[32], so is the quantification of a material opposition to current flow. In order to measure the surface resistivity of a material, it must be deposited as a film in the surface of an insulator, in this case quartz. In order to obtain this measuring, a four-point collinear probe, figure 3.12 is connected to a multimeter, figure 3.11.

Figure 3.12: Four-point collinear probe used with a zoom in on the probe identifying the four points.

Figure 3.11: Keithley 2450 sourcemeter used.

The four-point collinear probe has got four equally spaced probes, figure 3.12, then, the probes are placed over the material that is going to be measured, avoiding any lateral movement of the head to avoid damaging the material. The sourcemeter uses the points 1 and 4 to source a current through the sample, in the case of this study 1 mA, and the two inner probes measure the voltage drop between them.[33] In order to obtain the volume or bulk resistivity, ρ, the next equation is used:

$$\rho = \frac{\pi}{\ln 2} \frac{V}{I} tk \tag{3.1}$$

where:

- ρ = volume resistivity (Ω cm)
- V = voltage between probes 2 and 3 (V)
- I = magnitude of the source current (A)
- t = sample thickness (cm)
- k = correction factor

For materials as thin films, which are the ones measured in this work, sheet resistance or surface resistivity is determined and does not take thickness into account. The sheet resistance, σ, is

calculated using the next equation:

$$\sigma = \frac{\pi}{\ln 2}\frac{V}{I}k \tag{3.2}$$

where:

- σ = sheet resistance ($\Omega/\square$)

and the rest of symbols are the same as in equation 3.1.

The measurement obtained with the sourcemeter is σ which given in $\Omega/\square$. Is possible to obtain the volumetric resistivity as is expressed in the next equation:

$$\rho = \frac{\pi}{\ln 2}\frac{V}{I}tk \rightarrow \frac{\rho}{t} = \frac{\pi}{\ln 2}\frac{V}{I}k = \sigma \rightarrow \rho = t\sigma \tag{3.3}$$

3.2.4 Ultraviolet-visible spectroscopy (UV-spectroscopy)

Figure 3.13: Cary 50 Conc UV-Visible Spectrophotometer used.

Ultraviolet-visible molecular absorption spectroscopy[34] is a technique widely used in quantitative determination of the transmitance, T, or absorbance, A which both have adimensional units and are related between them according to the equation 3.4. Although it is mostly used with solutions, it can be used with non opaque solids such as graphene or multilayer graphene.

$$A = -\log T \tag{3.4}$$

In order to make the measurements, first, a clean quartz is put in the spectrophotometer, figure 3.13, and its absorbance Then, the different samples of quartz supported G-mats will be measured and compared and identify if any change appears in the absorption spectra.

3.2.5 X-ray photoelectron spectroscopy (XPS)

X-Ray Photoelectron Spectroscopy (XPS) is based on the photoelectric effect and consists in a photoemission process from a solid sample that interacts with an high energy photon (X-ray from 300 up to 1000 eV) and haves one electron removed from an atomic orbital that escapes into the vacuum. Then, the photoemission event takes place obeying the energy conservation rule[35][36], equation 3.5:

$$hv = E_B + E_{kin} \tag{3.5}$$

where:

- hv = photon energy
- E_B = electron binding energy relative to the vacuum.
- E_{kin} = kinetic energy of the photoelectron

The resulting spectra shows peaks with different binding energy. Each peak can be translated to different chemical states, for example, for C1s C-C has got a binding energy of 284.8 eV, C-O-C 286 eV and O-C=O 288.5 eV. This way, changes in the binding of the C that compose the G-mat can be identified.

3.3 Water splitting reaction tests

In this section are explained the experimental assebmly, the techniques used to carry out the water splitting reaction as well as the quantification of the produced hydrogen.

3.3.1 Experiment assembly

Figure 3.14: Potentiostat/Galvanostat used.

All electrochemical tests were performed in an AMETEK VersaSTAT 3 Potentiostat/Galvanostat, figure 3.14, using its software, VersaStudio 2.57.1. Once the photoelectrode is prepared it is mounted in a 3-electrode gas-tight electrochemical cell, figure 3.15, and the tests are performed. Hydrogen evolution was measured using an Agilent Technologies gas chromatograph model 7890A, figure 3.23.

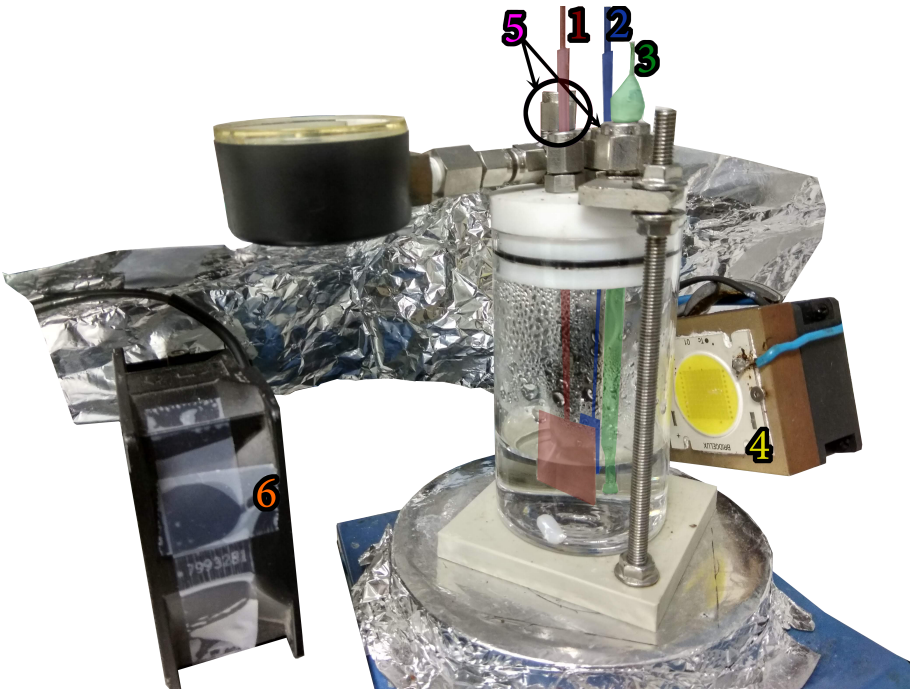

Figure 3.15: Electrochemical cell used. 1: Counter Electrode, 2: Working electrode, 3: Reference electrode, 4: Light source, 5: Gas purging entrance and gas venting and sample taking valve, 6: Cooling fan.

The electrochemical cell used is configured as a 3 electrode cell:

- Working electrode (WE): The photoelectrode prepared.
- Counter electrode (CE): A 2.5 cm x 2.5 cm x 0.1 cm platinum sheet.

- Reference electrode (Ref): Ag/AgCl saturated reference electrode[37].

The cell also has got a glass capillary that releases purging gas into the electrolyte and another steel capillary that serves as a gas venting valve during the purge. As electrolyte, 72 mL of 1 M Lithium perchlorate in 18.2 MΩ water was used, that after preparing the electrochemical cell for the experiment gets purged during 30 minutes with N_2 gas in order to remove all O_2 from the electrolyte. After the purge, the reactor is pressurized to 1.2 bar with N_2. The gas phase of the reactor is 134 mL, value obtained measuring the whole reactor, 206 mL, and then substracting the amount of electrolyte that is added.

The light source used is was a Bridgelux RS LED Array series model BXRA-50C5300-H-00 driven by a constant voltage power supply, figure 3.16. Its color temperature is 5000 K and it is close to 6000 lm at operating temperature. The LED emission spectra shows no emission in the UV region nor the IR region, meaning that all the radiation is in the visible region as can be seen in figure 3.17. The light source is placed at a distance of 5 cm parallel to the photoelectrode and the operating parameters of the power supply are:

- Voltage: 28.80 V (set).
- Forward current: Between 1.505 A and 1.490 A (measured current through the device, lowers varies a few mA during operation).

Figure 3.16: DC power supply used. Model EL303R branded by AimTTi.

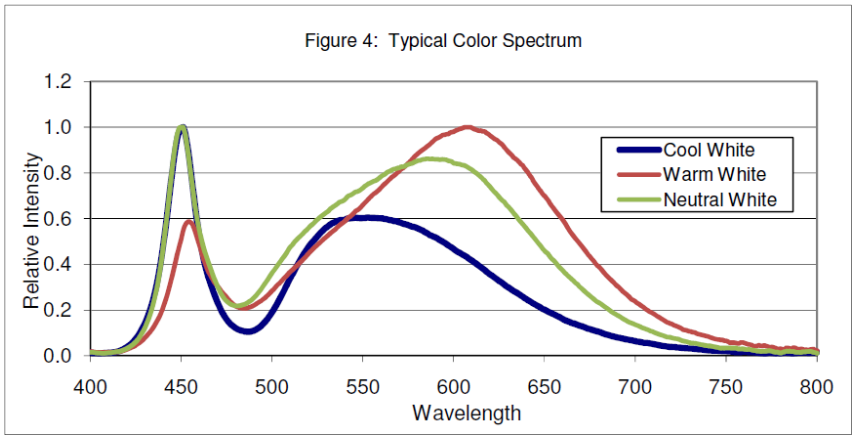

Figure 3.17: LED light source spectra, sourced from Bridgelux RS Array data sheet[38].

3.3.2 Electrochemical tests and parameters

In order to study the photoelectrodes, three electrochemical dynamic methods were used:

- Cyclic voltammetry
- Linear scan voltammetry
- Chronoamperometry

These have in common that they are controlled potential methods, meaning that the fixed value is the potential between the reference electrode and the working electrode. A current responds to the forced potential through the counter electrode. As can be seen in figure 3.18, potential (E_P) is fixed between the working electrode (WE) and the reference electrode (Ref); current (I) passes between the counter electrode (CE) and the working electrode.

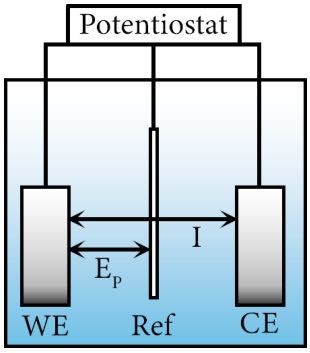

Figure 3.18: Schematic of a potentiostat operating a three electrode cell.

Cyclic voltammetry

Cyclic voltammetry[39] is an electrochemical method that forces a potential between two defined limits from an initial value at a given sweep sweep speed, figure 3.19 where E_0 is the initial potential, E_1 is the upper potential limit, E_2 is the lower potential limit and v the sweep speed. The parameters used are:

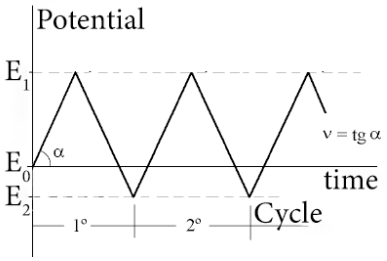

Figure 3.19: Evolution of a cyclic voltammetry potential during time.

- E_0 = -1.2 V vs Ag/AgCl sat.
- E_1 = 1.2 V vs Ag/AgCl sat.
- E_2 = -1.2 V vs Ag/AgCl sat.
- v = 0.1 Vs^{-1}

It is used in this work to check if the working electrode is able to force a charge separation and to verify the stability of the electrode. That is achieved by visual inspection of the resulting shape of the cyclic voltammetry. As can be seen in figure 3.20, the segment of the cyclic voltammetry that has raising potential does not overlap with the one that has decreasing potential.

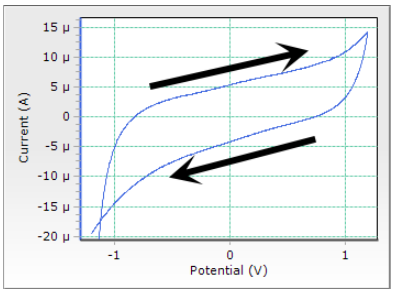

Figure 3.20: Example of a cyclic voltammetry.

Linear staircase voltammetry

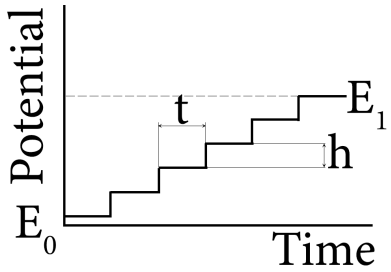

Figure 3.21: Potential evolution in a linear staircase voltammetry.

Linear staircase voltammetry[39] is a method that instead of applying a linear evolving potential, it raises the potential in steps with a delay between them as can be seen in figure 3.21 where E_0 is the starting potential, E_1 the ending potential, t the step time and h the step height. As the step time rises the behaviour of the system becomes closer to statonary. This method is used to compare the behaviour of the electrode between dark and light conditions. The parameters used during this work are:

- E_0 = 0 V vs Ag/AgCl sat.
- E_1 = -1.2 V vs Ag/AgCl sat.
- h = 25 mV
- t = 1 s

Chronoamperometry

Chronoamperometry is a fixed potential method where the measured variable is the current versus time at a given potential, figure 3.22. Although steps may be programmed in order to measure kinnetics of the reaction, in this work it is used monitor the current evolution during the experiment. The parameters used for this method during this work are:

- E_0 = -1.1 V vs Ag/AgCl sat.
- time = 4 hours

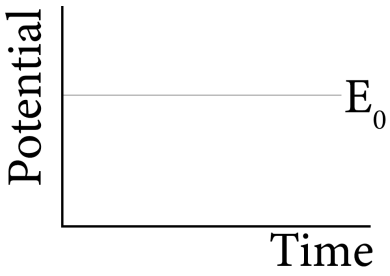

Figure 3.22: Potential evolution in a chronoamperometry.

3.3.3 Hydrogen quantification

Figure 3.23: Gas chromatograph used. Agilent Technologies model 7890A.

In order to quantify the hydrogen produced, 200 μL samples of the gas phase of the reactor were taken every hour. These samples were taken with a 200 μL Hamilton syringe and were introduced in an Agilent gas chromatograph model 7890A, figure 3.23. After running the gas chromatograph program, the H_2 peak was integrated in order to obtain its area. Then, the area was translated into a concentration according to the equation 3.6 that is obtained through the prior calibration with known amounts of hydrogen of the gas chromatograph.

$$Vol\%_{H_2} = \frac{Area - 10.210 \cdot 10^3}{8.829 \cdot 10^6} \tag{3.6}$$

Then, in order to transform the data to mol of hydrogen obtained a few assumptions are made:

- The gas behaves ideally.

- The temperature inside the reactor is 25 °C.
- The pressure difference after taking samples is insignificant.

Being these assumptions made, the amount of hydrogen generated is reflected in equation 3.7 using the ideal gas law.

$$n_{H_2} = \frac{P \cdot V}{R \cdot T} Vol\%_{H_2} \tag{3.7}$$

where:

- P is the pressure in Pa.
- V is the volume in m^3.
- n is the amount of moles of gas.
- R is the ideal gas constant in $J{\cdot}mol^{-1}{\cdot}K^{-1}$.
- T is the temperature of the gas in K.

As the only variable in the equation is Vol $\%_{H_2}$, the hydrogen produced is:

$$n_{H_2} = \frac{1.2 \cdot 10^5 Pa \cdot 134 \cdot 10^{-6} m^3}{8.314 J \cdot mol^{-1} \cdot K^{-1} \cdot 298.15 K} \cdot Vol\%_{H_2} = 6.487 \cdot 10^{-3} \cdot Vol\%_{H_2} \tag{3.8}$$

Chapter 4

Discussion of results

In this chapter, the results obtained are discussed. First of all, the characterization results will be presented. After the discussion of the characterization of the samples, the photoelectrochemical tests results are discussed. These results include the hydrogen produced at different times of the test (1 hour, 2 hours, 3 hours and 4 hours). At the end of each section of characterization the results are summarized.

4.1 Characterization

In this section, the characterization results will be discussed.

4.1.1 Atomic force microscopy

In this section, results of the atomic force microscopy are discussed.

G-mat without plasma treatment

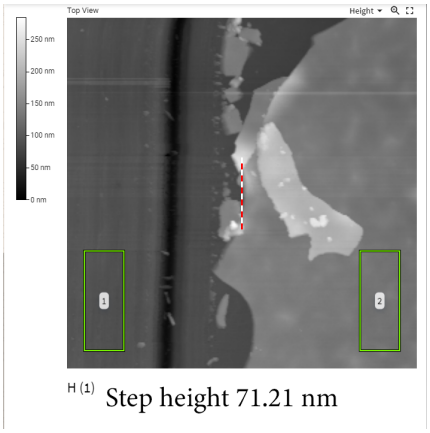

Figure 4.1: Regions (green rectangles) of scratched film used for measurement of the height of the sample without plasma treatment.

Atomic force microscopy of the G-mat sample that was not treated with oxygen plasma shows a film thickness of 71.21 nm, a root mean square height of the surface of 3.708 nm and a Kurtosis of height distribution of 3.32 nm. The figure 4.1 shows the regions of the scan that were used in order to measure the thickness of the film. Figure 4.2 shows a 3D image of the region used to measure the surface roughness parameters of the film.

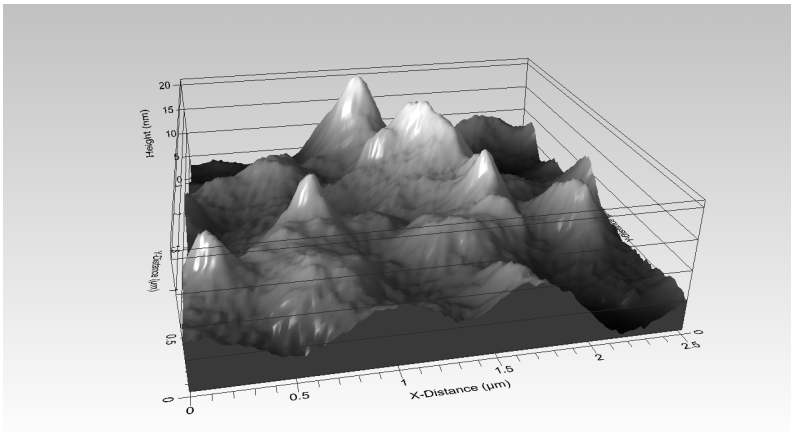

Figure 4.2: 3D AFM image of G-mat film without plasma treatment.

G-mat with 6 seconds of plasma treatment

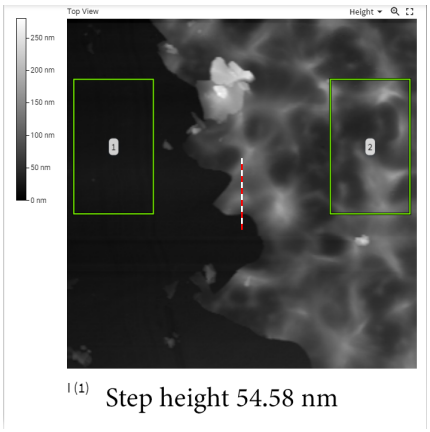

Figure 4.3: Regions (green rectangles) of scratched film used for measurement of the height of the sample with 6 seconds of plasma treatment.

Atomic force microscopy of the G-mat sample that was treated with oxygen plasma during 6 seconds shows a film thickness of 54.58 nm, a root mean square height of the surface of 24.91 nm and a Kurtosis of height distribution of 2.87 nm. The figure 4.3 shows the regions of the scan that were used in order to measure the thickness of the film. Figure 4.4 shows a 3D image of the region used to measure the surface roughness parameters of the film.

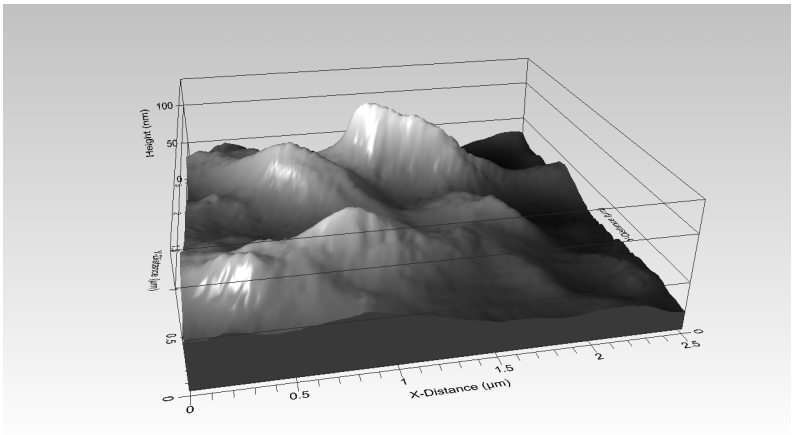

Figure 4.4: 3D AFM image of G-mat film with 6 seconds of plasma treatment.

G-mat with 12 seconds of plasma treatment

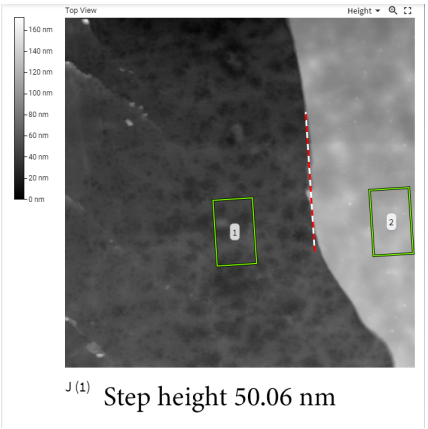

Figure 4.5: Regions (green rectangles) of scratched film used for measurement of the height of the sample with 12 seconds of plasma treatment.

Atomic force microscopy of the G-mat sample that was treated with oxygen plasma during 12 seconds shows a film thickness of 53.40 nm, a root mean square height of the surface of 3.07 nm and a Kurtosis of height distribution of 4.67 nm. The figure 4.3 shows the regions of the scan that were used in order to measure the thickness of the film. Figure 4.4 shows a 3D image of the region used to measure the surface roughness parameters of the film.

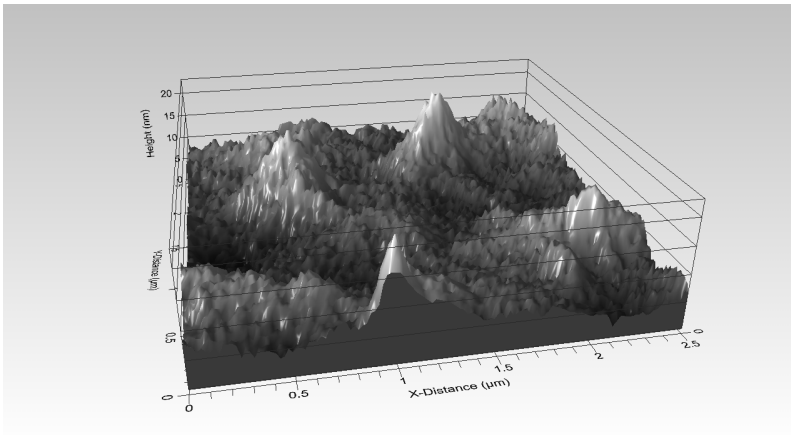

Figure 4.6: 3D AFM image of G-mat film with 12 seconds of plasma treatment.

G-mat with 18 seconds of plasma treatment

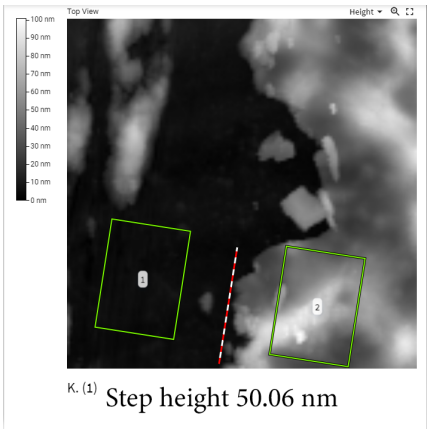

Figure 4.7: Regions (green rectangles) of scratched film used for measurement of the height of the sample with 18 seconds of plasma treatment.

Atomic force microscopy of the G-mat sample that was treated with oxygen plasma during 18 seconds shows a film thickness of 50.06 nm, a root mean square height of the surface of 19.46 nm and a Kurtosis of height distribution of 3.43 nm. The figure 4.7 shows the regions of the scan that were used in order to measure the thickness of the film. Figure 4.8 shows a 3D image of the region used to measure the surface roughness parameters of the film.

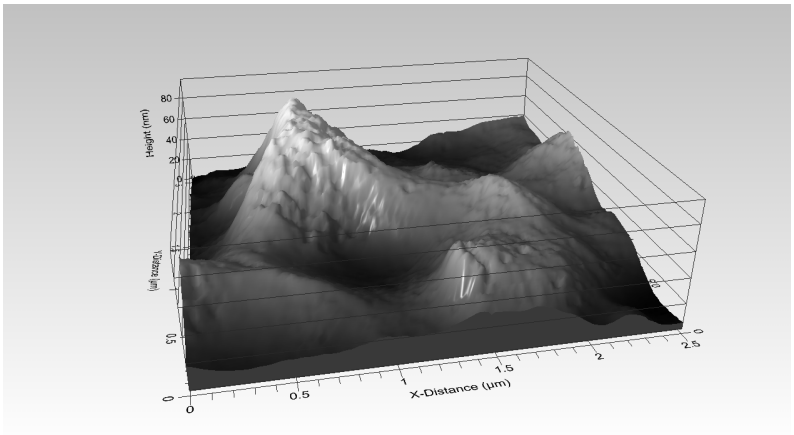

Figure 4.8: 3D AFM image of G-mat film with 18 seconds of plasma treatment.

Summary and discussion of atomic force microscopy results

The thickness values obtained are collected in table 4.1 and the surface roughness in table 4.2 and plotted in figure 4.9(a) and 4.9(b). Thickness seems to lower with the oxygen plasma treatment. This results seems logical, as oxygen plasma is an highly reactive form of oxygen and it is known to react with carbon[40]. Surface roughness results may be caused by the peeling off of the G-mat and the incorporation of defects and dangling bonds caused by the plasma treatment. With no plasma treatment, the surface of the G-mat has got a low roughness. Then, high reactive oxygen plasma starts to peel off the top layer of the G-mat, incorporating oxygen in the structure and removing carbon atoms in the form of CO_2 hereby generating dangling bonds. These defects in the structure causes the surface roughness that after completely peeling off a layer, the roughness lowers.

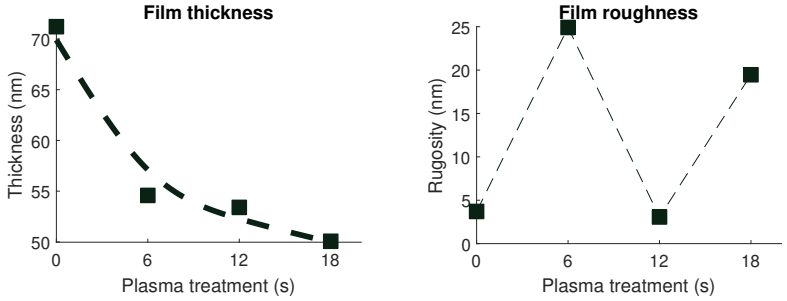

(a) Thickness (b) Roughness

Figure 4.9: Thickness and roughness evolution of the films for different plasma times.

Table 4.1: Summary of film thickness results.

Thickness					
Plasma:	**0 s**	**6 s**	**12 s**	**18 s**	**Units**
Thickness	71.21	54.58	53.40	50.06	nm

Table 4.2: Summary of film surface roughness results.

Area roughness					
Plasma:	**0 s**	**6 s**	**12 s**	**18 s**	**Units**
Sq	3.71	24.91	3.07	19.46	nm
Sku	3.32	2.87	4.67	3.43	-

4.1.2 Raman spectroscopy

In this section, results of Raman spectroscopy are discussed.

G-mat without plasma treatment

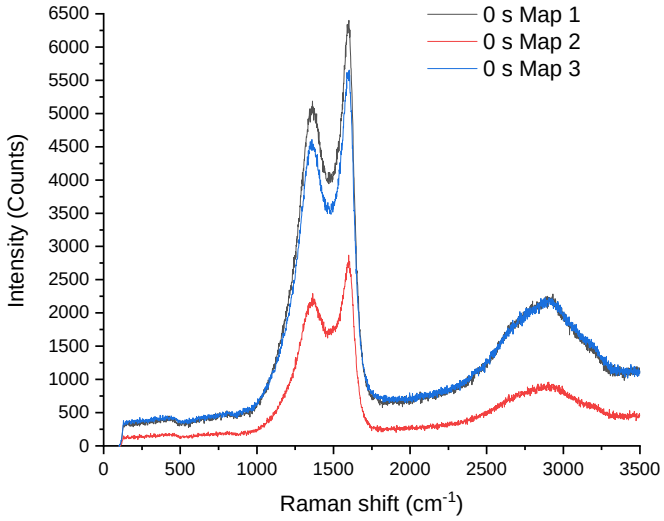

Figure 4.10: Raman spectra of G-mat sample without plasma treatment. 3 mappings. Each mapping is made in a different region of the same sample.

The Raman spectra of the G-mat sample without oxygen plasma treatment, figure 4.10, shows 2 well defined D and G peaks and a wide 2D region, which is expected for a multi-layer G-Mat. The G/D ratio, summarized in table 4.3, shows a value between 1.21 and 1.25, which are expected values for a defective G-mat film obtained from alginic acid.

Table 4.3: G-Mat without oxygen plasma treatment (0 s) D and G peaks counts and ratio.

0 s	**D**	**G**	**G/D**
Map 1	5187.44	6398.93	1.23
Map 2	2293.08	2869.76	1.25
Map 3	4608.09	5587.66	1.21
		Average	1.23

G-mat with 6 seconds of plasma treatment

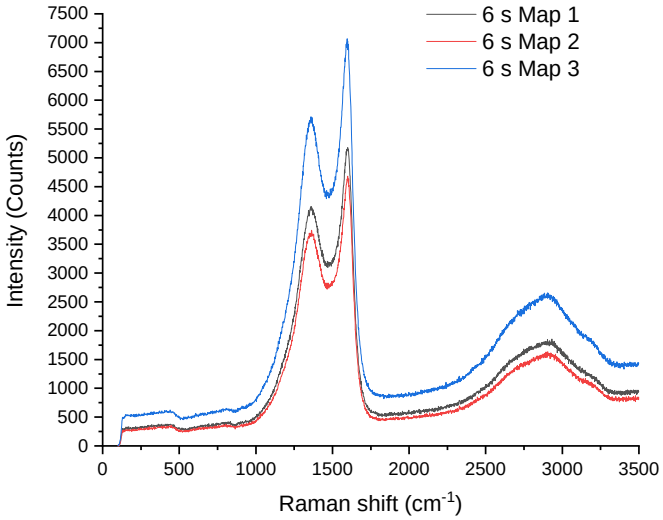

Figure 4.11: Raman spectra of G-mat sample with 6 seconds of plasma treatment. 3 mappings. Each mapping is made in a different region of the same sample.

The Raman spectra of the G-mat sample with 6 seconds of oxygen plasma treatment, figure 4.11, shows 2 well defined D and G peaks and a wide 2D region, which is expected for a multi-layer G-Mat. The G/D ratio, summarized in table 4.4, shows a value between 1.24 and 1.25, which are expected values for a defective G-mat film obtained from alginic acid.

Table 4.4: G-Mat with 6 seconds of oxygen plasma treatment D and G peaks counts and ratio.

6 s	**D**	**G**	**G/D**
Map 1	4156.87	5167.46	1.24
Map 2	3743.26	4680.88	1.25
Map 3	5699.233	7066.41	1.24
		Average	1.24

G-mat with 12 seconds of plasma treatment

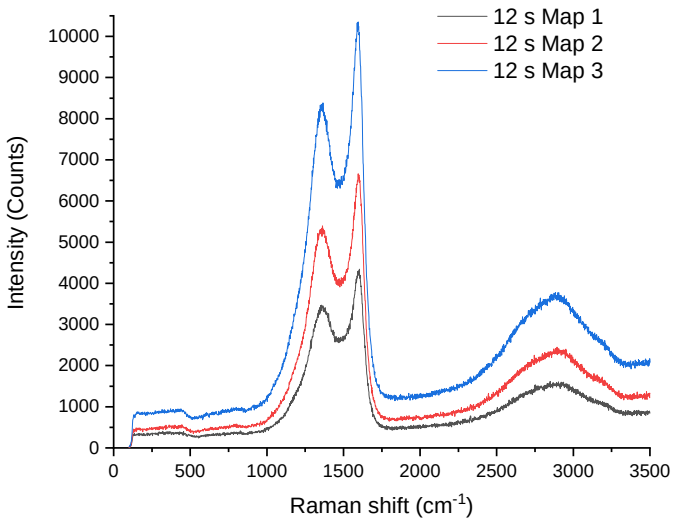

Figure 4.12: Raman spectra of G-mat sample with 12 seconds of plasma treatment. 3 mappings. Each mapping is made in a different region of the same sample.

The Raman spectra of the G-mat sample with 12 seconds of oxygen plasma treatment, figure 4.12, shows 2 well defined D and G peaks and a wide 2D region, which is expected for a multi-layer G-Mat. The G/D ratio, summarized in table 4.5, shows a value between 1.23 and 1.25, which are expected values for a defective G-mat film obtained from alginic acid.

Table 4.5: G-Mat with 12 seconds of oxygen plasma treatment D and G peaks counts and ratio.

6 s	**D**	**G**	**G/D**
Map 1	3468.15	4346.36	1.25
Map 2	5396.17	6660.47	1.23
Map 3	8383.73	10349.91	1.23
		Average	1.24

G-mat with 18 seconds of plasma treatment

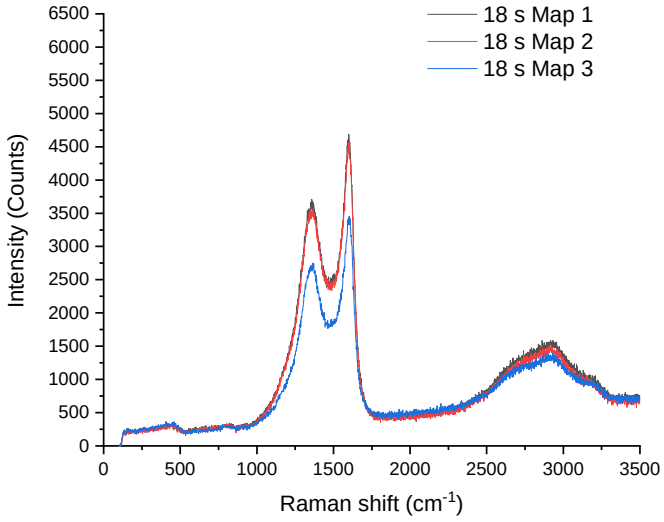

Figure 4.13: Raman spectra of G-mat sample with 18 seconds of plasma treatment. 3 mappings. Each mapping is made in a different region of the same sample.

The Raman spectra of the G-mat sample with 12 seconds of oxygen plasma treatment, figure 4.13, shows 2 well defined D and G peaks and a wide 2D region, which is expected for a multi-layer G-Mat. The G/D ratio, summarized in table 4.6, shows a value between 1.26 and 1.27, which are slightly higher than expected values for a defective G-mat film obtained from alginic acid.

Table 4.6: G-Mat with 18 seconds of oxygen plasma treatment D and G peaks counts and ratio.

18s	**D**	**G**	**G/D**
Map 1	3706.97	4689.99	1.27
Map 2	3620.83	4567.41	1.26
Map 3	2746.79	3455.36	1.26
		Average	1.26

Summary and discussion of Raman spectroscopy

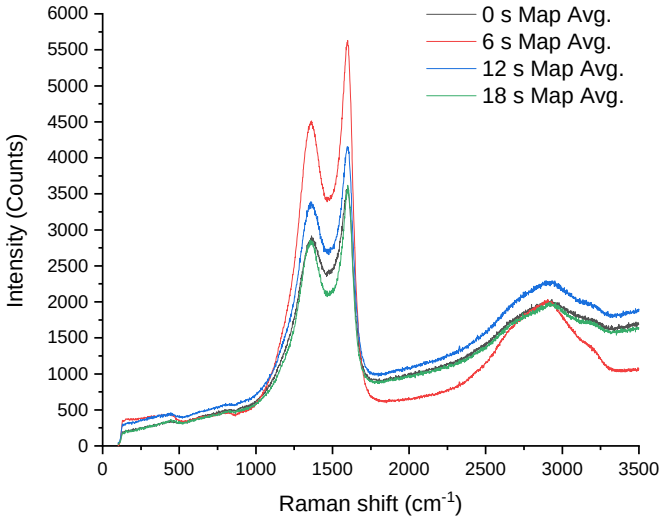

Figure 4.14: Raman spectra of the different G-mat samples. Average of the 3 mappings of each sample.

The Raman spectra of the different G-mat samples, figure 4.14, does not show any significant change in its spectra. The G/D ratio, summarized in table 4.7, shows a slightly increase in the G/D ratio after 18 seconds of treatment. For 6 and 12 seconds the change in the ratio is insignificant.

Table 4.7: D and G raman peaks values obtained from the mapping average of each sample and its G/D ratio.

Sample	D	G	G/D
0 s Avg.	2918.44	3611.52	1.24
6 s Avg.	4513.24	5628.38	1.25
12 s Avg.	3387.70	4155.94	1.23
18 s Avg.	2860.06	3618.77	1.27

4.1.3 Surface resistivity

In this section, the values of surface resistivity are discussed.

G-mat without plasma treatment

The obtained sheet resistance of the G-mat film without plasma treatment shows a sheet resistance between 4.3 and 5.3 $k\Omega\square^{-1}$ and as the film has got a thickness of 71.21 nm, a volume resistivity between 3.1 and 3.8 $\cdot 10^{-2}\Omega$ cm, table 4.8. This value is quite bigger than pristine graphene, around $10^{-6}\Omega$ cm, caused by the presence of impurities and stacking of layers.

Table 4.8: Resistivity of the G-mat sample without plasma treatment.

0 s	**Sheet resistance ($k\Omega\square^{-1}$)**	**Volume resistivity (Ω cm)**
1	4.360	$3.11\cdot10^{-2}$
2	5.251	$3.74\cdot10^{-2}$
3	4.449	$3.17E\cdot10^{-2}$

G-mat with 6 seconds of plasma treatment

The obtained sheet resistance of the G-mat film with 6 seconds of plasma treatment shows a sheet resistance between 4.7 and 5.7 $k\Omega\square^{-1}$ and as the film has got a thickness of 54.58 nm, a volume resistivity between 2.6 and 3.1 $\cdot 10^{-2}\Omega$ cm, table 4.9. It seems to have a slightly lower resistivity than the untreated one, although the difference is minimal.

Table 4.9: Resistivity of the G-mat sample with 6 seconds of plasma treatment.

6 s	**Sheet resistance ($k\Omega\square^{-1}$)**	**Volume resistivity (Ω cm)**
1	4.781	$2.61\cdot10^{-2}$
2	5.644	$3.08E\cdot10^{-2}$
3	4.894	$2.67E\cdot10^{-2}$

G-mat with 12 seconds of plasma treatment

The obtained sheet resistance of the G-mat film with 12 seconds of plasma treatment shows a sheet resistance between 5.4 and 6.8 $k\Omega\square^{-1}$ and as the film has got a thickness of 53.40 nm, a volume resistivity between 2.9 and 3.6 $\cdot 10^{-2}\Omega$ cm, table 4.10. It seems to have a slightly lower resistivity than the untreated one and slightly higher than the one treated for 6 second in oxygen plasma, although the difference is minimal.

Table 4.10: Resistivity of the G-mat sample with 12 seconds of plasma treatment.

12 s	**Sheet resistance ($k\Omega\square^{-1}$)**	**Volume resistivity (Ω cm)**
1	5.456	$2.91\cdot10^{-2}$
2	6.784	$3.62\cdot10^{-2}$
3	5.611	$3.00\cdot10^{-2}$

G-mat with 18 seconds of plasma treatment

The obtained sheet resistance of the G-mat film with 18 seconds of plasma treatment shows a sheet resistance between 9.0 and 12.8 $k\Omega\square^{-1}$ and as the film has got a thickness of 50.06 nm, a volume resistivity between 5.6 and 6.41 $\cdot 10^{-2}\Omega$ cm, table 4.11. It seems to have a slightly higher resistivity than the rest of the samples.

Table 4.11: Resistivity of the G-mat sample with 18 seconds of plasma treatment.

18 s	**Sheet resistance ($k\Omega\square^{-1}$)**	**Volume resistivity (Ω cm)**
1	12.810	$6.41 \cdot 10^{-2}$
2	9.092	$4.55 \cdot 10^{-2}$
3	11.207	$5.61 \cdot 10^{-2}$

Summary and discussion of resistance results

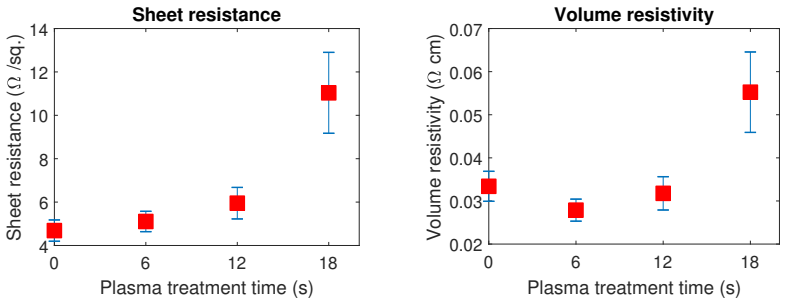

(a) Sheet resistance

(b) Volume resistivity

Figure 4.15: Sheet resistance and volume resistivity evolution of the samples for different plasma treatment times.

As can be seen in the figures 4.15(a), the sheet resistance of the film raises as longer plasma treatment times are used this can be caused due to oxidation of G-mat surface as well as the thinning down of the film. Figure 4.15(b) shows that the volume resistivity, which varies in function of the thickness of the film, of the G-mat experiences a decrease in its resistivity during the first 6 seconds of the plasma treatment and then it raises again. A possible explanation for this behavior can be that during the first 6 seconds of plasma treatment, the highly reactive oxygen plasma can be reacting with the first defective layer of the graphene, thus with higher resistivity, and is exposing a less defective layer which posseses a lower resistivity. Then, the highly reactive oxygen plasma starts to raise the amount of defects and so does its volume resistivity.

4.1.4 Ultraviolet-visible spectroscopy

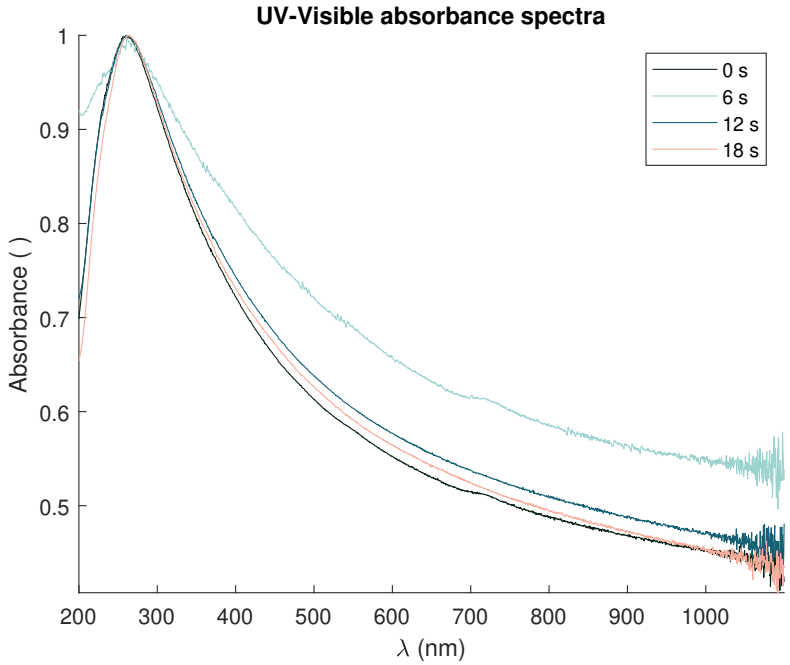

Figure 4.16: Normalized UV-Visible absorbance spectra of the different G-mat samples, absorbance of quartz corrected.

The resulting spectra, figure 4.16 shows the same peaks for all the samples and its shape is the same as the one expected for a non-pristine graphene [41]. Although the 6 s sample shows slightly more flattened peak, the difference can be caused due to a slightly more thick region of the film or a slight inclination in the film assembly in the spectrophotometer, causing a thicker optical path. Therefore, all the samples UV-visible absorption spectra can be considered equal.

4.1.5 X-ray photoelectron spectroscopy

In this section, X-ray photoelectron spectroscopy results are discussed.

G-mat without plasma treatment

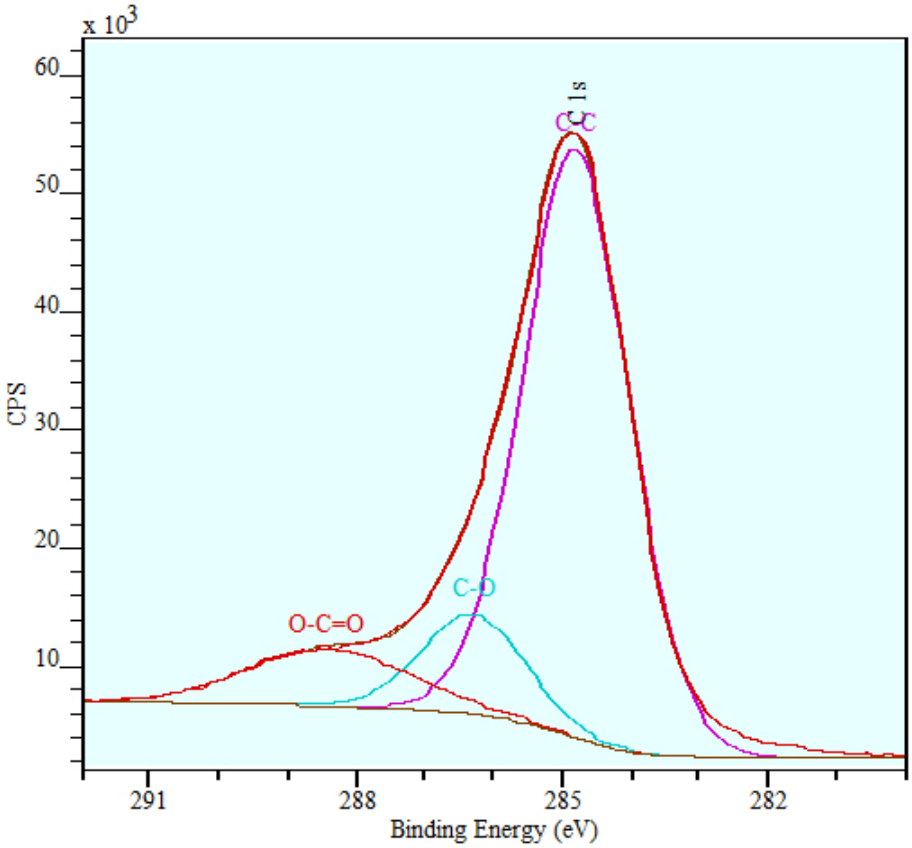

Figure 4.17: Deconvoluted XPS of the sample without plasma treatment.

The deconvolution of the XPS C 1s peak, figure 4.17, shows that the main bond in the material is C-C, as is expected for a G-mat. The presence of oxygen bonds in the sample is caused due to the precursor used to prepare the G-mat is rich hydroxil and carboxyl groups.

Table 4.12: Carbon bond percentage for the sample without plasma treatment determined by XPS.

Sample	C-C	C-O	O-C=O
0 s	75.94 at.%	12.41 at.%	11.66 at.%

G-mat with 6 seconds of plasma treatment

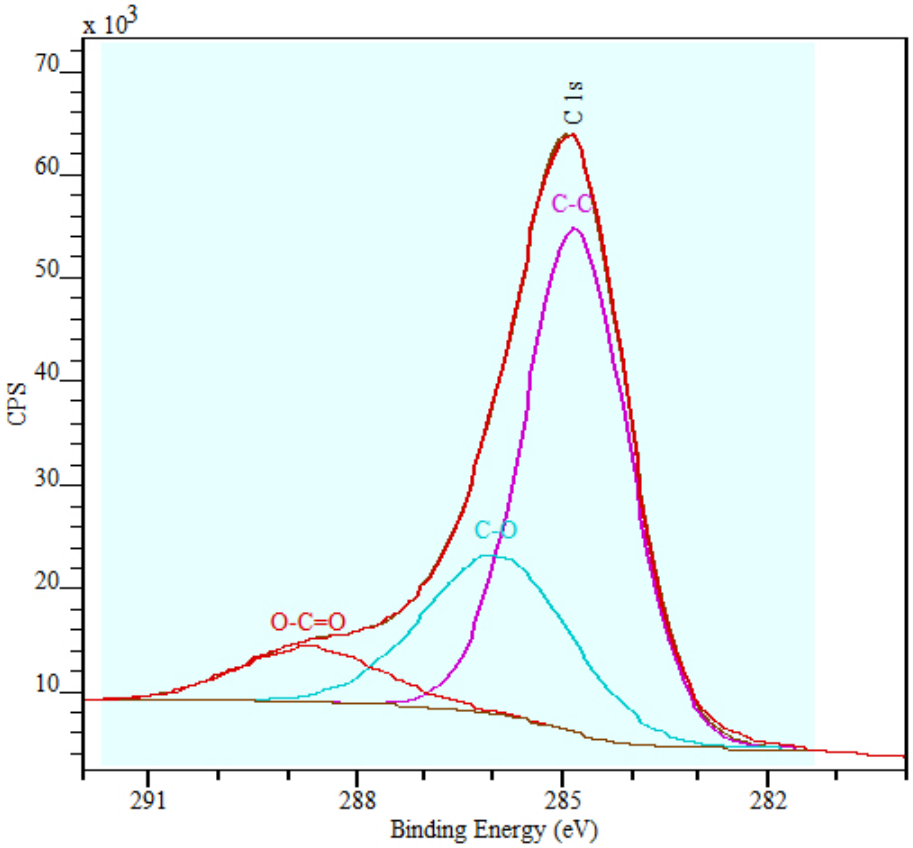

Figure 4.18: Deconvoluted XPS of the sample with 6 seconds of plasma treatment.

The deconvolution of the XPS C 1s peak, figure 4.18, shows a decrease in the amount of C-C bonds and a clear increase in the C-O bonds respect the sample without plasma treatment. This results seems to indicate that the oxygen plasma may be setting in the structure forming bonds with the carbon, although in the other techniques were no clear evidences.

Table 4.13: Carbon bond percentage for the sample with 6 seconds of plasma treatment determined by XPS.

Sample	C-C	C-O	O-C=O
6 s	62.64 at.%	27.78 at.%	9.58 at.%

G-mat with 12 seconds of plasma treatment

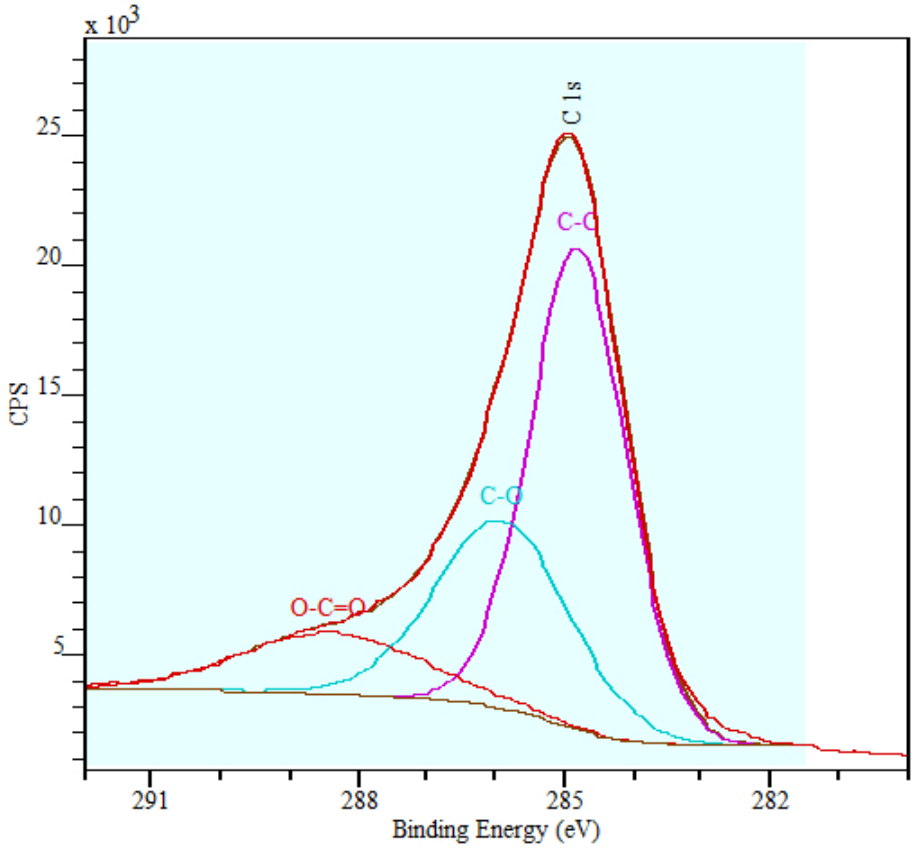

Figure 4.19: Deconvoluted XPS of the sample with 12 seconds of plasma treatment.

The deconvolution of the XPS C 1s peak, figure 4.19, shows a decrease in the amount of C-C bonds and a clear increase in the C-O bonds respect the sample without plasma treatment, as happened with 6 seconds of plasma treatment.

Table 4.14: Carbon bond percentage for the sample with 12 seconds of plasma treatment determined by XPS.

Sample	C-C	C-O	O-C=O
12 s	55.87 at.%	30.29 at.%	13.84 at.%

G-mat with 18 seconds of plasma treatment

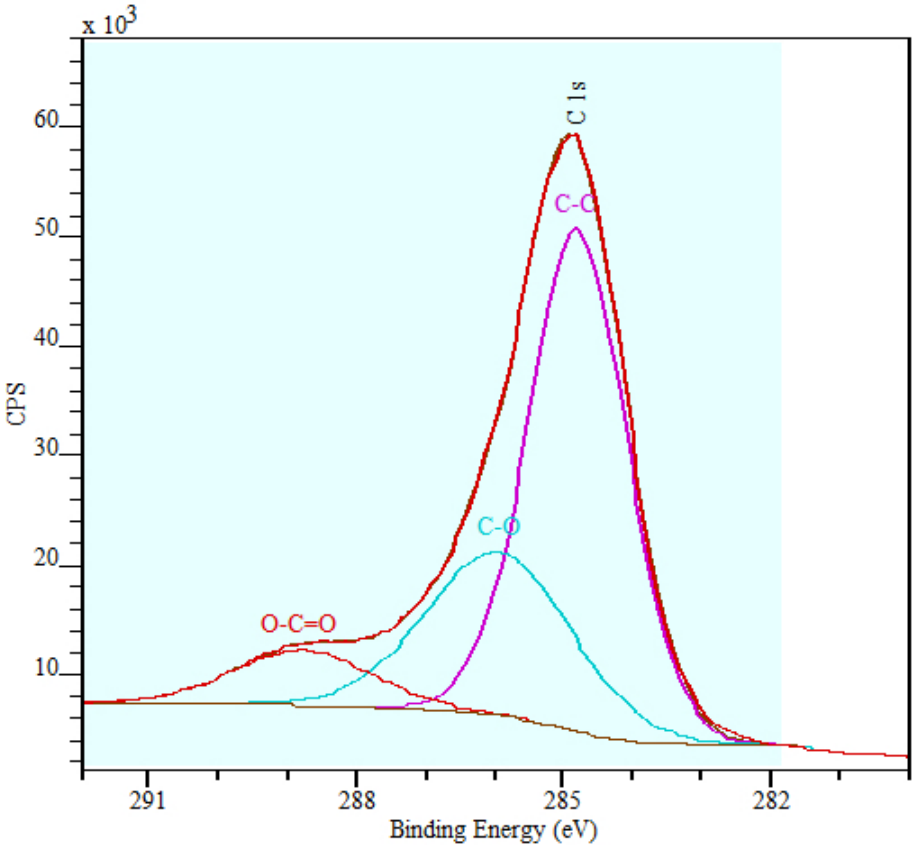

Figure 4.20: Deconvoluted XPS of the sample with 18 seconds of plasma treatment.

The deconvolution of the XPS C 1s peak, figure 4.20, shows a decrease in the amount of C-C bonds and a clear increase in the C-O bonds respect the sample without plasma treatment, table 4.15, as happened with 6 and 12 seconds of plasma treatment.

Table 4.15: Carbon bond percentage for the sample with 18 seconds of plasma treatment determined by XPS.

Sample	C-C	C-O	O-C=O
18 s	61.14 at.%	29.32 at.%	9.55 at.%

Summary and discussion of X-ray photoelectron spectroscopy results

Table 4.16: Summary of carbon bond percentage for the different samples determined by XPS.

Sample	C-C	C-O	O-C=O
0 s	75.94 at.%	12.41 at.%	11.66 at.%
6 s	62.64 at.%	27.78 at.%	9.58 at.%
12 s	55.87 at.%	30.29 at.%	13.84 at.%
18 s	61.14 at.%	29.32 at.%	9.55 at.%

The values summarized in table 4.16 are represented in figure 4.21 as percentage of bonds versus duration of plasma treatment. There can be seen that the amount of C-C bonds lowers fast during the first 6 seconds of treatment and then it stays close to that value. In the case of C-O bonds a similar behaviour is seen, they raise to a value close to 30 % and stays over time at that percentage. In other hand, the case of the O-C=O bonds does not show any significant change over time.

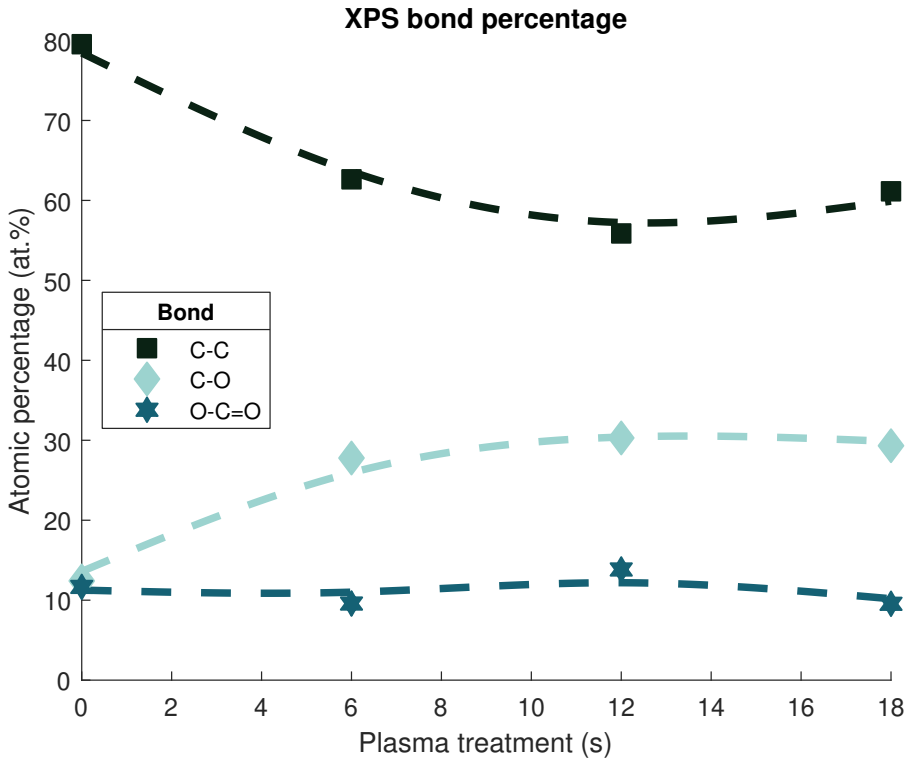

Figure 4.21: Evolution of C-C, C-O and O-C=O bonds over different plasma treatment times.

4.2 Photoelectrochemical tests

4.2.1 Sample without plasma treatment - chronoamperometry with light irradiation.

As expected, a film with very few defects is non photoreactive, so the sample without any treatment does not show any notable change in the linear scan voltammetry current density when it is irradiated with visible light, figure 4.22.

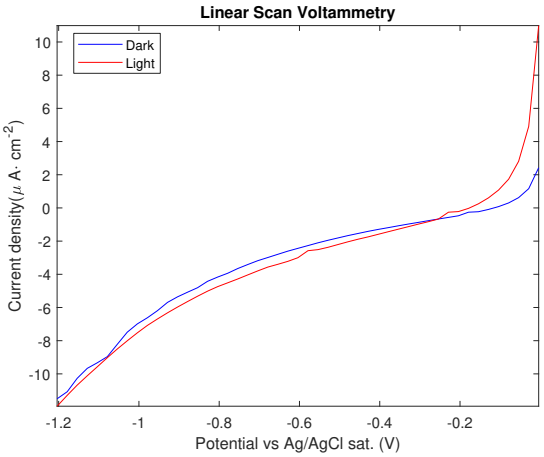

Figure 4.22: Linear scan voltammetry under light and dark conditions of the sample without plasma treatment.

Figure 4.23 shows the cyclic voltammetry of the sample without plasma treatment before (*Initial*) and after (*End*) the electrocatalytic tests. There is no change in the shape of the voltammetry, although there is an increase in the current density after the 4 hours of chronoamperometry. A possible explanation for this behaviour can be the activation of the surface of the electrode after 4 hours at -1.1 V vs Ag/AgCl.

The current evolution of the chronoamperometry is shown in figure 4.24. No abrupt changes in the current can be observed. There is a change over time in the current density which, in absolute value, raises. This is coherent with the cyclic voltammetry results. Figure 4.25 shows that no hydrogen was produced during the experiment, exact amount collected at table 4.17.

Table 4.17: Hydrogen production over time for the sample without plasma treatment with light irradiation.

Sample	**μmol cm^{-2} at 1 h**	**μmol cm^{-2} at 2 h**	**μmol cm^{-2} at 3 h**	**μmol cm^{-2} at 4 h**
0 s	0	0	0	0

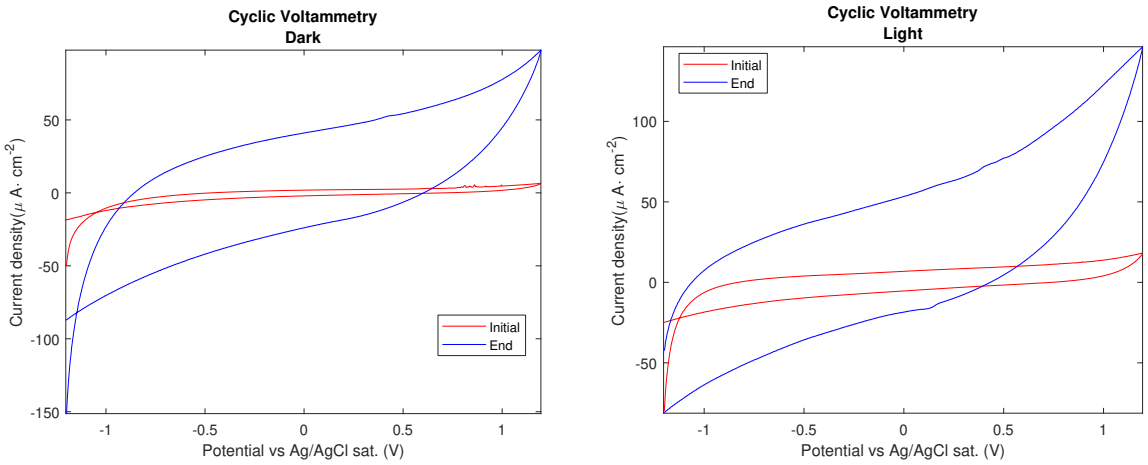

(a) Dark.

(b) Light.

Figure 4.23: Cyclic voltammetry of the sample without plasma treatment before and after the chronoamperometry.

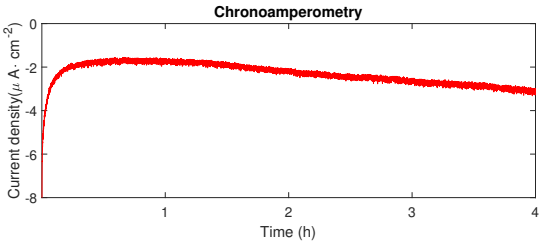

Figure 4.24: Chronoamperometry of the sample without plasma treatment irradiated with light.

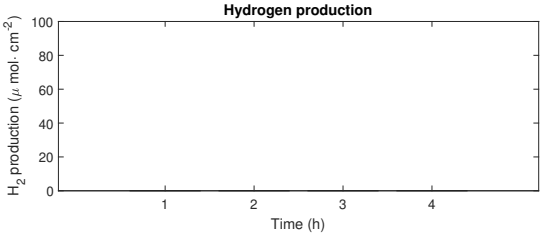

Figure 4.25: Hydrogen production over time for the sample without plasma treatment with light irradiation.

4.2.2 Sample without plasma treatment - chronoamperometry without light irradiation.

Figure 4.26(a) shows the cyclic voltammetry of a fresh sample without plasma treatment and with no irradiation of light before (*Initial*) and after (*End*) the electrocatalytic tests, figure 4.26(b). There is no change in the shape of the voltammetry, although there is an increase in the current density after the 4 hours of chronoamperometry. A possible explanation for this behaviour can be the activation of the surface of the electrode after 4 hours at -1.1 V vs Ag/AgCl as happened with the other sample. Some abrupt changes can be seen during the chronoamperometry. These changes coincide with the sampling of gas and are caused by the slight movement of the reactor.

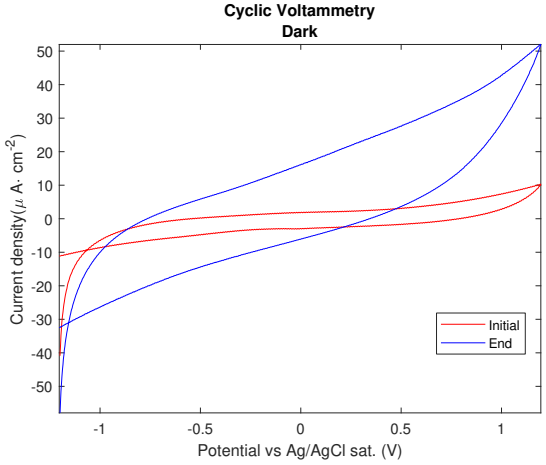

(a) Cyclic voltammetry before and after chronoamperometry.

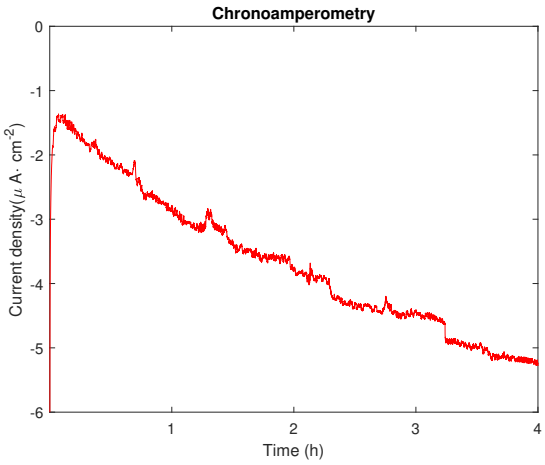

(b) Chronoamperometry.

Figure 4.26: Cyclic voltammetry and chronoamperometry of a fresh sample without plasma treatment.

Figure 4.27 shows that no hydrogen was produced during the experiment, exact amount collected at table 4.18.

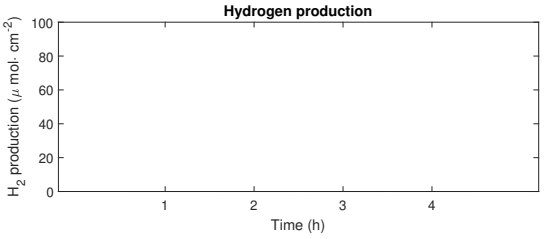

Figure 4.27: Hydrogen production over time for the sample without plasma treatment without light irradiation.

Table 4.18: Hydrogen production over time for the sample without plasma treatment without light irradiation.

Sample	**μmol cm^{-2} at 1 h**	**μmol cm^{-2} at 2 h**	**μmol cm^{-2} at 3 h**	**μmol cm^{-2} at 4 h**
0 s *Dark*	0	0	0	0

4.2.3 Sample with 6 seconds of plasma treatment - chronoamperometry with light irradiation.

The first sample with 6 seconds of plasma treatment shows a slight change in the linear scan voltammetry current density when it is irradiated with visible light, figure 4.28. As the current density difference between the two experiments at -1.1 V vs Ag/AgCl, -0.901 V vs NHE, is notable, this potential was the one set to perform all the experiments.

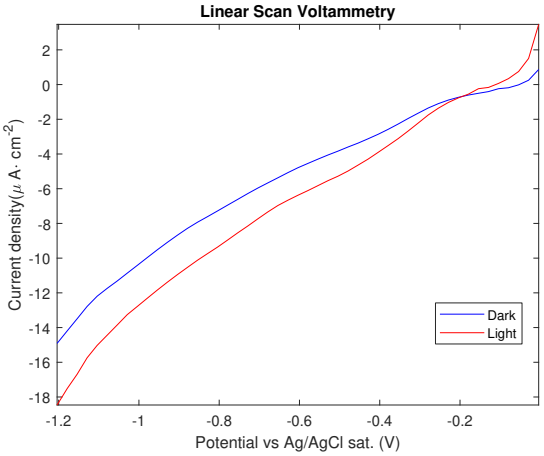

Figure 4.28: Linear scan voltammetry under light and dark conditions of the first sample with 6 seconds of plasma treatment.

Figure 4.29 shows the cyclic voltammetry of the sample with 6 seconds of plasma treatment before (*Initial*) and after (*End*) the electrocatalytic tests. There is no change in the shape of the voltammetry, although there is an increase in the current density after the 4 hours of chronoamperometry. A possible explanation for this behaviour can be the activation of the surface of the electrode after 4 hours at -1.1 V vs Ag/AgCl as happens with the other samples.

The current evolution of the chronoamperometry is shown in figure 4.30. No abrupt changes in the current is present. There is a change over time in the current density which, in absolute value, raises. This is coherent with the cyclic voltammetry results. Figure 4.31 shows that hydrogen was produced during the experiment, exact amount collected in table 4.19.

Table 4.19: Hydrogen production over time for the first sample with 6 seconds of plasma treatment with light irradiation.

Sample	**μmol cm^{-2} at 1 h**	**μmol cm^{-2} at 2 h**	**μmol cm^{-2} at 3 h**	**μmol cm^{-2} at 4 h**
6 s *First*	0.134	20.046	40.531	85.640

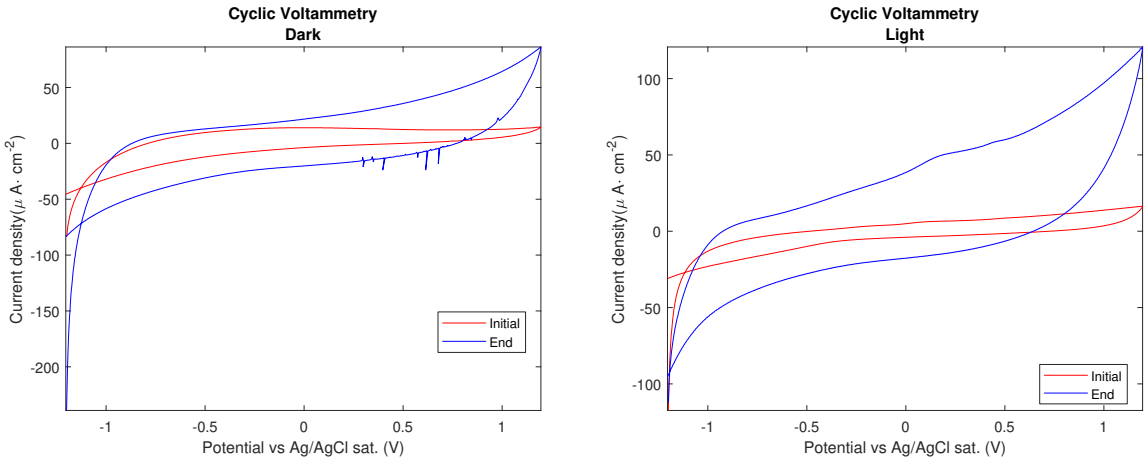

(a) Dark.

(b) Light.

Figure 4.29: Cyclic voltammetry of the first sample with 6 seconds of plasma treatment before and after the chronoamperometry.

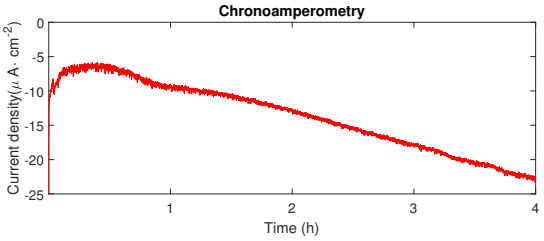

Figure 4.30: Chronoamperometry of the first sample with 6 seconds of plasma treatment irradiated with light.

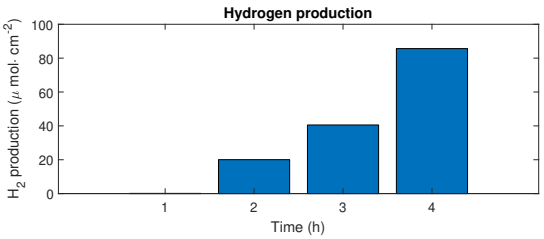

Figure 4.31: Hydrogen production over time for the sample with 6 seconds of plasma treatment with light irradiation.

4.2.4 Sample with 6 seconds of plasma treatment - chronoamperometry without light irradiation.

Figure 4.32(a) shows the cyclic voltammetry of a fresh sample with 6 seconds of plasma treatment and with no irradiation of light before (*Initial*) and after (*End*) the electrocatalytic tests, figure 4.32(b). There is no change in the shape of the voltammetry, although there is an increase in the current density after the 4 hours of chronoamperometry. A possible explanation for this behaviour can be the activation of the surface of the electrode after 4 hours at -1.1 V vs Ag/AgCl as happened with the other sample. No abrupt changes are seen during the chronoamperometry.

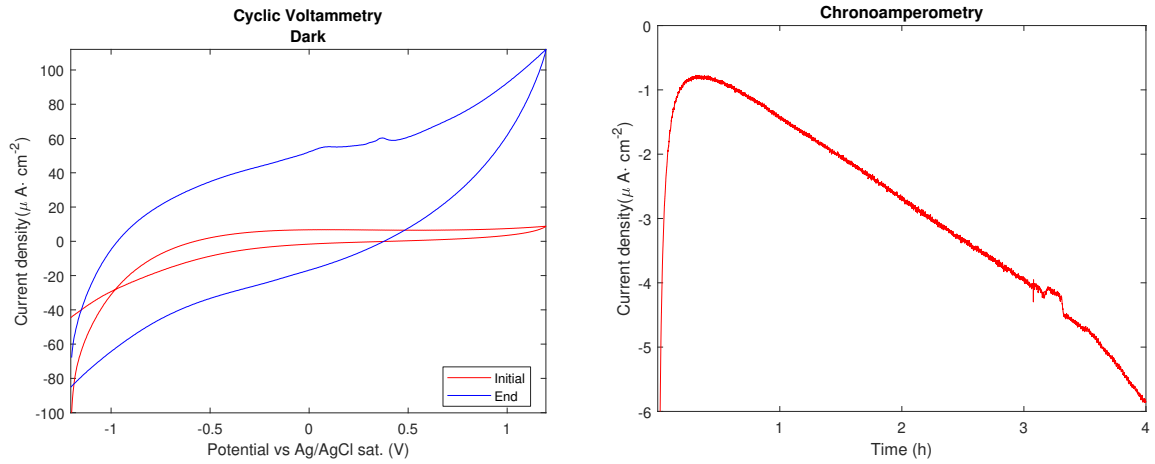

(a) Cyclic voltammetry before and after chronoamperometry.

(b) Chronoamperometry.

Figure 4.32: Cyclic voltammetry and chronoamperometry of a fresh sample with 6 seconds of plasma treatment without light irradiation.

An insignificant amount of hydrogen was produced during this experiment as is shown in figure 4.33 and collected in table 4.20.

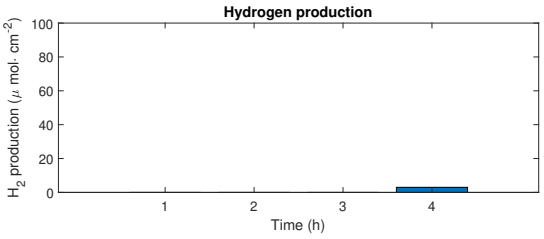

Figure 4.33: Hydrogen production over time for the sample with 6 seconds of plasma treatment without light irradiation.

Table 4.20: Hydrogen production over time for the sample with 6 seconds of plasma treatment without light irradiation.

Sample	**μmol cm^{-2} at 1 h**	**μmol cm^{-2} at 2 h**	**μmol cm^{-2} at 3 h**	**μmol cm^{-2} at 4 h**
6 s *Dark*	0	0	0	3.002

4.2.5 Sample with 12 seconds of plasma treatment - chronoamperometry with light irradiation.

The sample with 12 seconds of plasma treatment shows a slight change in the linear scan voltammetry current density when it is irradiated with visible light, figure 4.34.

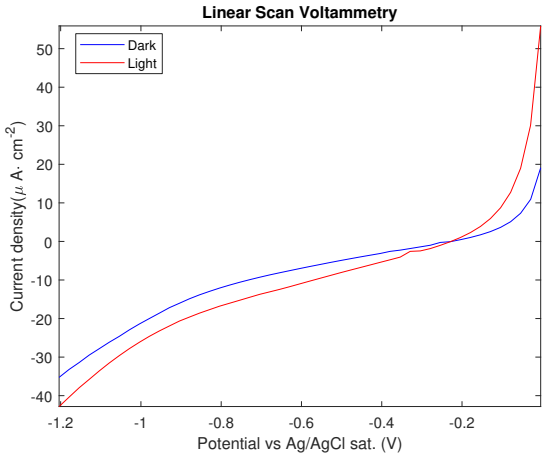

Figure 4.34: Linear scan voltammetry under light and dark conditions of the sample with 12 seconds of plasma treatment.

Figure 4.35 shows the cyclic voltammetry of the sample with 12 seconds of plasma treatment before (*Initial*) and after (*End*) the electrocatalytic tests. There is no change in the shape of the voltammetry, although there is an increase in the current density after the 4 hours of chronoamperometry. A possible explanation for this behaviour can be the activation of the surface of the electrode after 4 hours at -1.1 V vs Ag/AgCl as happens with the other samples.

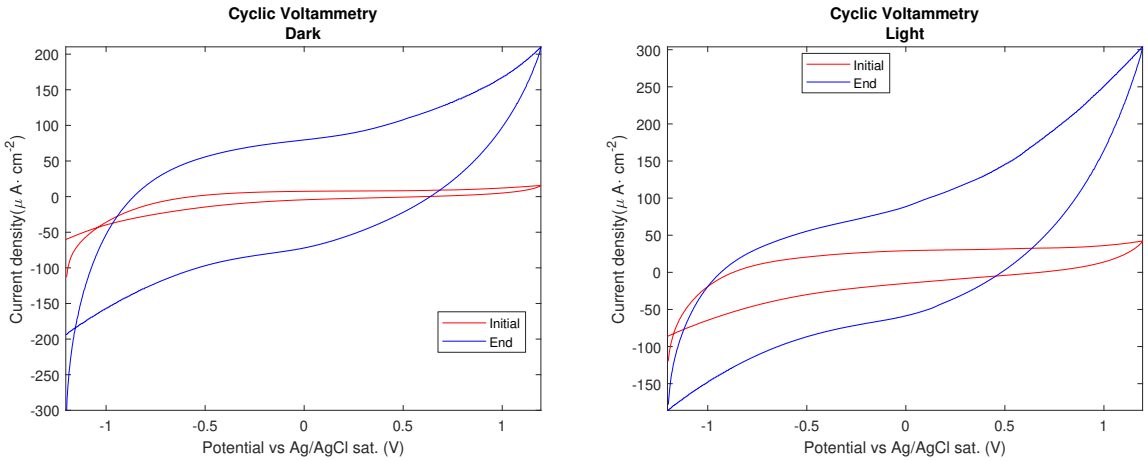

(a) Dark.

(b) Light.

Figure 4.35: Cyclic voltammetry of the second sample with 12 seconds of plasma treatment before and after the chronoamperometry.

The current evolution of the chronoamperometry is shown in figure 4.36. No abrupt changes in the current is present. There is a change over time in the current density which, in absolute value, raises. This is coherent with the cyclic voltammetry results. Table 4.21 shows that hydrogen was produced during the experiment.

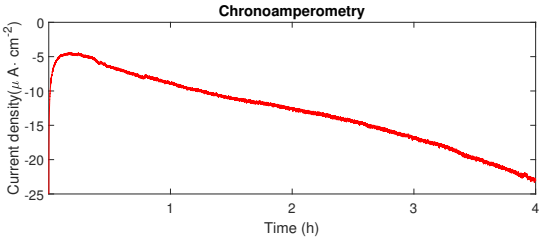

Figure 4.36: Chronoamperometry of the sample with 12 seconds of plasma treatment irradiated with light.

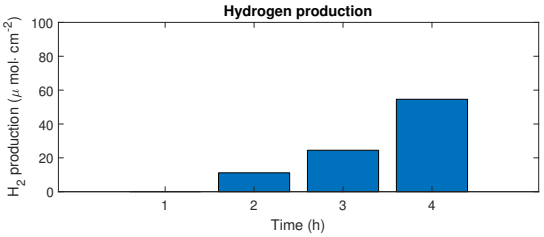

Figure 4.37: Hydrogen production over time for the sample with 12 seconds of plasma treatment with light irradiation.

Table 4.21: Hydrogen production over time for the sample with 12 seconds of plasma treatment with light irradiation.

Sample	**μmol cm^{-2} at 1 h**	**μmol cm^{-2} at 2 h**	**μmol cm^{-2} at 3 h**	**μmol cm^{-2} at 4 h**
12 s	0	11.156	24.491	54.592

4.2.6 Sample with 12 seconds of plasma treatment - chronoamperometry without light irradiation.

Figure 4.38(a) shows the cyclic voltammetry of a fresh sample with 12 seconds of plasma treatment and with no irradiation of light before (*Initial*) and after (*End*) the electrocatalytic tests, figure 4.38(b). In this case, two strange peaks appear in the cyclic voltammetry before and after the chronoamperometry. This behaviour is caused by contamination of the sample or degradation of the reference electrode, as is a strange peak that does not appear before. Also, as happened with the other samples there is an increase in the current density after the 4 hours of chronoamperometry that can be explained due to the activation of the surface of the electrode after 4 hours. No abrupt changes are seen during the chronoamperometry.

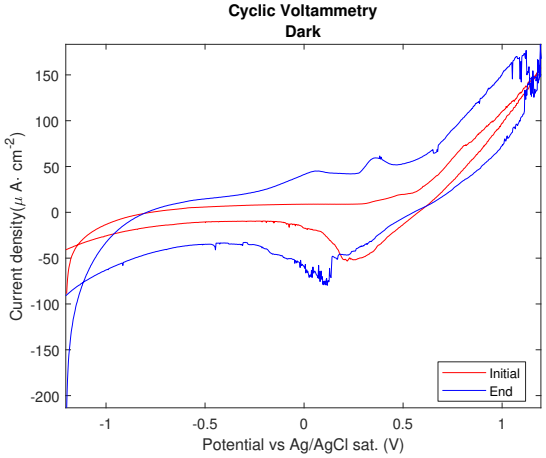

(a) Cyclic voltammetry before and after chronoamperometry.

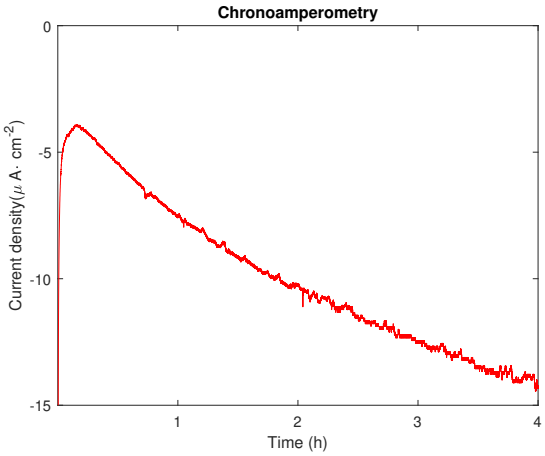

(b) Chronoamperometry.

Figure 4.38: Cyclic voltammetry and chronoamperometry of a fresh sample with 12 seconds of plasma treatment without light irradiation.

A small amount of hydrogen was produced during this experiment as is shown in figure 4.39, exact data values collected at table 4.22. Although the presence of the strange peaks and the possibility of contamination forces to discard this result.

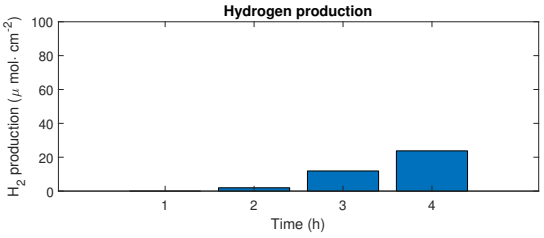

Figure 4.39: Hydrogen production over time for the sample with 12 seconds of plasma treatment without light irradiation.

Table 4.22: Hydrogen production over time for the sample with 6 seconds of plasma treatment without light irradiation. Marked with an * as the truthfulness of the results of this experiment are in doubt.

Sample	μmol cm^{-2} at 1 h	μmol cm^{-2} at 2 h	μmol cm^{-2} at 3 h	μmol cm^{-2} at 4 h
12 s $_{Dark}$*	0	1.957	11.884	23.759

4.2.7 Sample with 18 seconds of plasma treatment - chronoamperometry with light irradiation.

The sample with 18 seconds of plasma treatment shows an insignificant change in the linear scan voltammetry current density when it is irradiated with visible light, figure 4.40.

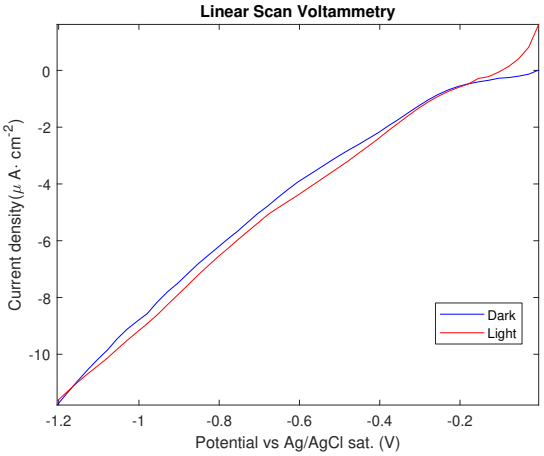

Figure 4.40: Linear scan voltammetry under light and dark conditions of the sample with 12 seconds of plasma treatment.

Figure 4.41 shows the cyclic voltammetry of the sample with 18 seconds of plasma treatment before (*Initial*) and after (*End*) the electrocatalytic tests. There is no change in the shape of the voltammetry, although there is an increase in the current density after the 4 hours of chronoamperometry. A possible explanation for this behaviour can be the activation of the surface of the electrode after 4 hours at -1.1 V vs Ag/AgCl as happens with the other samples.

The current evolution of the chronoamperometry is shown in figure 4.42. No abrupt changes in the current is present. There is a change over time in the current density which, in absolute value, raises. This is coherent with the cyclic voltammetry results. Figure 4.43 shows that no hydrogen was produced during the experiment, exact values collected at table 4.23.

Table 4.23: Hydrogen production over time for the sample with 18 seconds of plasma treatment with light irradiation.

Sample	μmol cm^{-2} at 1 h	μmol cm^{-2} at 2 h	μmol cm^{-2} at 3 h	μmol cm^{-2} at 4 h
18 s	0	0	0	0

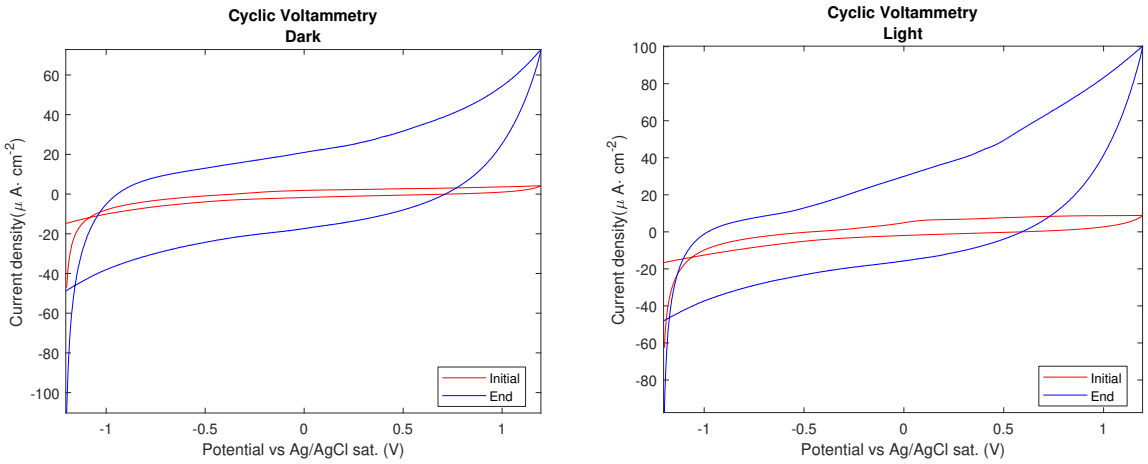

(a) Dark.

(b) Light.

Figure 4.41: Cyclic voltammetry of the second sample with 18 seconds of plasma treatment before and after the chronoamperometry.

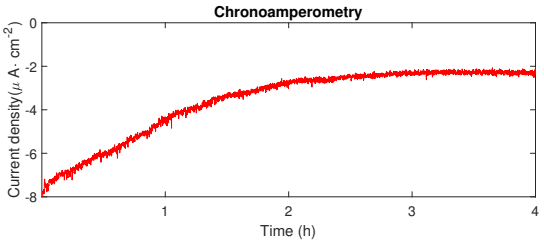

Figure 4.42: Chronoamperometry of the sample with 18 seconds of plasma treatment irradiated with light.

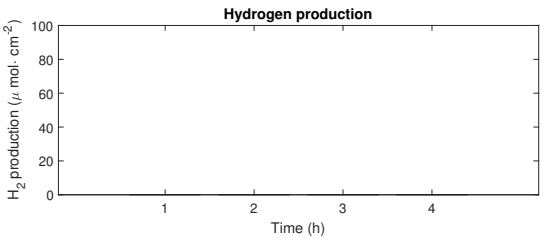

Figure 4.43: Hydrogen production over time for the sample with 18 seconds of plasma treatment with light irradiation.

4.2.8 Summary and discussion of the photoelectrochemical tests

In this section the hydrogen production results are collected in table 4.24 shown in figure 4.44. In the figure, the samples without oxygen plasma treatment, 6 seconds of plasma treatmet without light irradiation treatment and 18 s of plasma treatment with light irradiation are overlapped in the bottom of the figure. **The greatest amount of hydrogen is produced by the films treated during 6 seconds with oxygen plasma and with light irradiation**. The film treated with 12 seconds of plasma oxygen irradiated with light shows a lower production of hydrogen. The results of the film with 12 seconds of plasma treatment and without light irradiation are to be ignored because the lack of truthfulness of its results as are discussed in its section. Of these results can be concluded that the best films are produced treating the films during 6 seconds in oxygen plasma and that visible light promotes the photoelectrocatalytic production of hydrogen. For greater plasma times, the benefits are diminished or completely vanished.

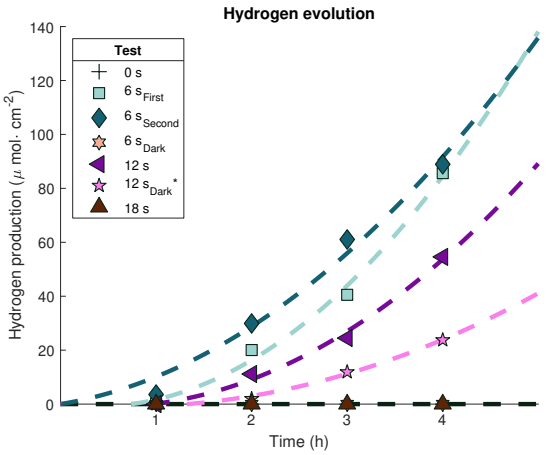

Figure 4.44: Hydrogen evolution for the different experiments.

Table 4.24: Summary of hydrogen production over time for all the samples.

Sample	μmol cm^{-2} at 1 h	μmol cm^{-2} at 2 h	μmol cm^{-2} at 3 h	μmol cm^{-2} at 4 h
0 s	0	0	0	0
0 s *Dark*	0	0	0	0
6 s *First*	0.134	20.046	40.531	85.640
6 s *Second*	3.554	29.904	61.057	88.924
6 s *Dark*	0	0	0	3.002
12 s	0	11.156	24.491	54.592
12 s *Dark**	0	1.957	11.884	23.759
18 s	0	0	0	0

Chapter 5

Conclusions

Multilayer-graphene was obtained through pyrolisis of alginic acid and treated with oxygen plasma for different amounts of time. The films were characterized and the different techniques revealed different characteristics of the produced materials:

- Atomic force microscopy shown that plasma treatment had an effect on the thickness of the films. They became thinner after oxygen plasma treatment due to, presumably, the production of carbon dioxide with the outer layers of the G-mat. Oxygen plasma treatment had no clear tendency over its surface roughness as some samples had higher rugosity and others lower.
- Raman spectroscopy demonstrated that the different G-mats had the characteristic peaks of a graphenic material, D and G peak, and its 2D region was wide, which indicates that the material has many layers stacked.
- Surface resistivity test revealed that the oxygen plasma treatment increased the sheet resistance of the material but when its results were merged with the thickness acquired in atomic force microscopy, volume resistivity showed that for short times of plasma treatment lowered.
- Ultraviolet-visible absorbance shown that the absorbance spectra of the different G-mats had no changes and its absorption was approximately the same for the different oxygen plasma treatment times.
- X-ray photoelectron spectroscopy revealed after its deconvolution that the material bond ratio changed after the oxygen plasma treatment, lowering its amount of C-C bonds and increasing the amount of C-O bonds. The amount of carboxyl groups hovered around the same value no matter the duration of the plasma treatment.

The effect of oxygen plasma can be observed through the different characterization techniques. When high reactivity oxygen reacts with the outer layers of the G-mat, it starts to reacts with the layers through the incorporation of oxygen in the structure, producing defects and carbon dioxide or monoxide and as a result of the loss of layers the thickness lowers. These defects alter the ratio

of C-C and C-O bonds, reducing the first but keeping the defective-graphene structure as shown in the Raman spectra and UV-visible absorbance spectra. The increase in defects, corroborated by the C-O bond and Raman G/D ratio, translates into an increase of active sites for catalysis but also an increase its sheet resistance that lowers its effectiveness as an electrode.

The experimental assembly used to test the photoelectrodes shown valid results and the amount of hydrogen produced depending of its oxygen plasma treatment, being 6 seconds the best duration for the treatment for photoelectrocatalytic hydrogen production. The best sample was repeated in order to validate its result and experiments without light were also performed to validate the effect of the light in the hydrogen production.

Although low amounts of hydrogen were produced, the working conditions were far from the ideal. This work was performed in a neutral electrolyte and the photoelectrode was irradiated only with visible light. Optimal working conditions for this reaction are an acidic media and UV-visible irradiation. Further studies of this material should be done under better reaction conditions in order to improve its productivity.

Bibliography

[1] British Petroleum. "BP Statistical Review of World Energy 2017". In: *British Petroleum* 66 (2017), pp. 1–52. ISSN: 1098-6596. DOI: http://www.bp.com/content/dam/bp/en/corporate/pdf/energy-economics/statistical-review-2017/bp-statistical-review-of-world-energy-2017-full-report.pdf. arXiv: arXiv:1011.1669v3. URL: https://www.bp.com/content/dam/bp/en/corporate/pdf/energy-economics/statistical-review-2017/bp-statistical-review-of-world-energy-2017-full-report.pdfhttps://www.bp.com/content/dam/bp/en/corporate/pdf/energy-economics/statistical-review-2017/bp-statistic (cit. on p. 3).

[2] NASA. *Climate Change: Vital Signs of the Planet: Evidence* (cit. on p. 4).

[3] Tom Boden, Bob Andres, and Gregg Marland. *Global Greenhouse Gas Emissions Data*. Tech. rep. Carbon Dioxide Information Analysis Center, 2017, U.S. Department of Energy, Oak Ridge, Tennessee. DOI: 10.3334/CDIAC/00001_V2017. URL: http://cdiac.ess-dive.lbl.gov/trends/emis/tre{_}glob{_}2014.htmlcdiac.esd.ornl.gov/trends/emis/top2014.cap (cit. on p. 4).

[4] Devens Gust, Thomas A. Moore, and Ana L Moore. "Solar fuels via artificial photosynthesis". In: *Accounts of Chemical Research* 42.12 (2009), pp. 1890–1898. ISSN: 00014842. DOI: 10.1021/ar900209b. URL: http://pubs.acs.org/doi/pdf/10.1021/ar900209b (cit. on p. 5).

[5] Hydrogen Fuel Cell Engines and Related Technologies. "Module 1: Hydrogen Properties". In: *Hydrogen Fuel Cell Engines* (2001), p. 41. URL: https://energy.gov/sites/prod/files/2014/03/f12/fcm01r0.pdfhttp://www1.eere.energy.gov/hydrogenandfuelcells/tech{_}validation/pdfs/fcm01r0.pdf (cit. on p. 6).

[6] Ramchandra Bhandari, Clemens A. Trudewind, and Petra Zapp. "Life cycle assessment of hydrogen production via electrolysis - A review". In: *Journal of Cleaner Production* 85 (2014), pp. 151–163. ISSN: 09596526. DOI: 10.1016/j.jclepro.2013.07.048. URL: https://www.sciencedirect.com/science/article/pii/S095965261300509X (cit. on p. 6).

[7] National Research Council (U.S.). Committee on Alternatives and Strategies for Future Hydrogen Production and Use., National Academy of Engineering., and National Academy of Sciences (U.S.) *The hydrogen economy : opportunities, costs, barriers, and R & D needs*. National Academies Press, 2004, p. 239. ISBN: 9780309091633. URL: https://books.google.es/books?id=frebvNJnFpIC{\&}pg=PA85{\&}lpg=PA85{\&}dq=air+products+48{\%}25+natural+gas+30{\%}25+oil+18{\%}25+coal+4{\%}25+electrolysis{\&}source=bl{\&}ots=bQ6LMm3ji9{\&}sig=ACfU3U0{_}g0HIz5eBhWvk9BeWWabUwomkBA{\&}hl=en{\&}sa=X{\&}ved=2ahUKEwi1t7rFraXkAhWS34UKHWb{_}BkAQ6AEwAHo (cit. on p. 6).

[8] Mari Voldsund, Kristin Jordal, and Rahul Anantharaman. "Hydrogen production with CO2 capture". In: *International Journal of Hydrogen Energy* 41.9 (2016), pp. 4969–4992. ISSN: 03603199. DOI: 10.1016/j.ijhydene.2016.01.009. URL: https://linkinghub.elsevier.com/retrieve/pii/S0360319915312659 (cit. on p. 6).

[9] International Energy Agency. *Energy Technology Perspectives 2012*. 2012, p. 382. ISBN: 9789264174887. DOI: 10.1787/energy_tech-2012-en. URL: http://www.iea.org/termsandconditionsuseandcopyright/http://www.oecd-ilibrary.org/energy/energy-technology-perspectives-2012{_}energy{_}tech-2012-en (cit. on p. 6).

[10] Pavlos Nikolaidis and Andreas Poullikkas. "A comparative overview of hydrogen production processes". In: *Renewable and Sustainable Energy Reviews* 67 (2017), pp. 597–611. ISSN: 18790690. DOI: 10.1016/j.rser.2016.09.044. URL: https://ac.els-cdn.com/S1364032116305366/1-s2.0-S1364032116305366-main.pdf?{_}tid=6a5ab160-0508-11e8-8ed1-00000aab0f6c{\&}acdnat=1517239614{_}ea65cfd495630d6e9609543e7250f56bhttp://dx.doi.org/10.1016/j.rser.2016.09.044 (cit. on p. 7).

[11] Akira Fujishima and Kenichi Honda. "Electrochemical photolysis of water at a semiconductor electrode". In: *Nature* 238.5358 (1972), pp. 37–38. ISSN: 00280836. DOI: 10.1038/238037a0. arXiv: arXiv:1011.1669v3. URL: http://www.nature.com/doifinder/10.1038/238037a0 (cit. on p. 8).

[12] Ryu Abe. *Z-Scheme Type Water Splitting into H2and O2Under Visible Light Through Two-Step Photoexcitation Between Two Different Photocatalysts*. Elsevier B.V., 2013, pp. 341–370. ISBN: 9780444538727. DOI: 10.1016/B978-0-444-53872-7.00016-9. URL: http://dx.doi.org/10.1016/B978-0-444-53872-7.00016-9 (cit. on p. 8).

[13] Josny Joy, Jinu Mathew, and Soney C. George. "Nanomaterials for photoelectrochemical water splitting – review". In: *International Journal of Hydrogen Energy* 43.10 (2018), pp. 4804–4817. ISSN: 03603199. DOI: 10.1016/j.ijhydene.2018.01.099. URL: https://www.sciencedirect.com/science/article/abs/pii/S0360319918301745 (cit. on p. 10).

[14] Ryu Abe. *Recent progress on photocatalytic and photoelectrochemical water splitting under visible light irradiation*. 2010. DOI: 10.1016/j.jphotochemrev.2011.02.003. URL: https://ac.els-cdn.com/S1389556711000050/1-s2.0-S1389556711000050-main.

pdf?{_}tid=3d37fffe-0575-11e8-b086-00000aacb35d{\&}acdnat=1517286362{_}aba990c9ea6268d7f6c01e6665841ac3 (cit. on p. 10).

[15] A. K. Geim. "Graphene: Status and prospects". In: *Science* 324.5934 (2009), pp. 1530–1534. ISSN: 00368075. DOI: 10.1126/science.1158877. arXiv: 0906.3799 (cit. on p. 10).

[16] Matthew J. Allen, Vincent C. Tung, and Richard B. Kaner. "Honeycomb carbon: A review of graphene". In: *Chemical Reviews* 110.1 (2010), pp. 132–145. ISSN: 00092665. DOI: 10.1021/cr900070d. URL: https://pubs.acs.org/doi/10.1021/cr900070d (cit. on p. 10).

[17] Sergio Navalon et al. "Carbocatalysis by graphene-based materials". In: *Chemical Reviews* 114.12 (2014), pp. 6179–6212. ISSN: 15206890. DOI: 10.1021/cr4007347 (cit. on p. 10).

[18] William S. Hummers and Richard E. Offeman. "Preparation of Graphitic Oxide". In: *Journal of the American Chemical Society* 80.6 (1958), p. 1339. ISSN: 15205126. DOI: 10.1021/ja01539a017. URL: https://pubs.acs.org/doi/abs/10.1021/ja01539a017 (cit. on p. 11).

[19] Yi Zhang, Luyao Zhang, and Chongwu Zhou. "Review of chemical vapor deposition of graphene and related applications". In: *Accounts of Chemical Research* 46.10 (2013), pp. 2329–2339. ISSN: 00014842. DOI: 10.1021/ar300203n. URL: https://pubs.acs.org/doi/10.1021/ar300203n (cit. on p. 11).

[20] Cristina Lavorato et al. "N-doped graphene derived from biomass as a visible-light photocatalyst for hydrogen generation from water/methanol mixtures". In: *Chemistry - A European Journal* 20.1 (2014), pp. 187–194. ISSN: 09476539. DOI: 10.1002/chem.201303689 (cit. on p. 12).

[21] Alejandra Garcia, Josep Albero, and Hermenegildo García. "Multilayer N-doped Graphene Films as Photoelectrodes for H 2 Evolution". In: *ChemPhotoChem* 1.9 (2017), pp. 388–392. ISSN: 23670932. DOI: 10.1002/cptc.201700049. URL: http://doi.wiley.com/10.1002/cptc.201700049 (cit. on p. 12).

[22] Alejandra García et al. "Graphenes as additives in photoelectrocatalysis". In: *J. Mater. Chem. A* (2017). ISSN: 2050-7488. DOI: 10.1039/C7TA04045H. URL: http://pubs.rsc.org/en/content/articlepdf/2017/ta/c7ta04045hhttp://xlink.rsc.org/?DOI=C7TA04045H (cit. on p. 12).

[23] Marcos Latorre-Sánchez, Ana Primo, and Hermenegildo García. "P-doped graphene obtained by pyrolysis of modified alginate as a photocatalyst for hydrogen generation from water-methanol mixtures". In: *Angewandte Chemie - International Edition* 52.45 (2013), pp. 11813–11816. ISSN: 14337851. DOI: 10.1002/anie.201304505 (cit. on p. 12).

[24] Wenchao Tian et al. "A review on lattice defects in graphene: Types generation effects and regulation". In: *Micromachines* 8.5 (2017), p. 163. ISSN: 2072666X. DOI: 10.3390/mi8050163. URL: http://www.mdpi.com/2072-666X/8/5/163 (cit. on p. 12).

[25] Sonia Remiro-Buenamañana and Hermenegildo García. *Photoassisted CO2 Conversion to Fuels*. 2019. DOI: 10.1002/cctc.201801409. URL: https://onlinelibrary.wiley.com/doi/abs/10.1002/cctc.201801409 (cit. on p. 12).

[26] Shou En Zhu, Shengjun Yuan, and G. C.A.M. Janssen. "Optical transmittance of multilayer graphene". In: *EPL* 108.1 (2014), p. 17007. ISSN: 12864854. DOI: 10.1209/0295-5075/108/17007. URL: http://stacks.iop.org/0295-5075/108/i=1/a=17007?key=crossref.616c8d071423614 7f07e767339d82a3b (cit. on p. 13).

[27] Diego Mateo, Josep Albero, and Hermenegildo García. "Photoassisted methanation using Cu2O nanoparticles supported on graphene as a photocatalyst". In: *Energy and Environmental Science* 10.11 (2017), pp. 2392–2400. ISSN: 17545706. DOI: 10.1039/c7ee02287e. URL: http://xlink.rsc.org/?DOI=C7EE02287E (cit. on p. 13).

[28] L. E. Scriven. "Physics and Applications of DIP Coating and Spin Coating". In: *MRS Proceedings* 121 (1988), p. 717. ISSN: 0272-9172. DOI: 10.1557/PROC-121-717. URL: https://www.cambridge.org/core/product/identifier/S1946427400485180/type/journal{_}article (cit. on p. 18).

[29] Ana Primo et al. "Graphenes in the absence of metals as carbocatalysts for selective acetylene hydrogenation and alkene hydrogenation". In: *Nature Communications* 5.1 (2014), p. 5291. ISSN: 20411723. DOI: 10.1038/ncomms6291. URL: http://www.nature.com/articles/ncomms6291 (cit. on p. 18).

[30] Gary M. McClelland, Ragnar Erlandsson, and Shirley Chiang. "Atomic Force Microscopy: General Principles and a New Implementation". In: *Review of Progress in Quantitative Nondestructive Evaluation*. Boston, MA: Springer US, 1987, pp. 1307–1314. DOI: 10.1007/978-1-4613-1893-4_148. URL: http://link.springer.com/10.1007/978-1-4613-1893-4{_}148 (cit. on pp. 20, 21).

[31] J. B. *Symmetry and spectroscopy; an introduction to vibrational and electronic spectroscopy*. Vol. 62. Dover Publications, 1980, p. 301. ISBN: 9780486661445. DOI: 10.1016/0022-2860(80)85247-1 (cit. on p. 21).

[32] E. Alfredo Campo. "Physical Properties of Polymeric Materials". In: *Selection of Polymeric Materials*. William Andrew Publishing, 2008, pp. 175–203. ISBN: 978-0-8155-1551-7. DOI: 10.1016/b978-081551551-7.50007-3. URL: https://www.sciencedirect.com/science/article/pii/B9780815515517500061{\#}cesec61 (cit. on p. 21).

[33] Tektronix. "Application Note Series Resistivity Measurements Using the Model 2450 SourceMeter SMU Instrument and a Four-Point Collinear Probe" (cit. on p. 22).

[34] Douglas A. Skoog, Stanley R. Crouch, and F.James Holler. *Instrumental Analysis Principles (7th Ed.)* 2016, p. 1056. ISBN: 0495125709 (cit. on p. 23).

[35] Elettra Sincrotrone Trieste. *X-ray Photoelectron Spectroscopy*. URL: http://www.elettra.trieste.it/lightsources/labs-and-services/surface-lab/x-ray-photoelectron-spectroscopy.html (visited on 06/05/2019) (cit. on p. 23).

[36] ThermoFisher. *Thermo Scientific XPS: What is XPS*. 2019. URL: https://xpssimplified.com/whatisxps.php (visited on 06/05/2019) (cit. on p. 23).

[37] Timothy J Smith and Keith J Stevenson. *Reference Electrodes*. Elsevier B.V., 2007, pp. 73–110. DOI: 10.1016/B978-0-444-51958-0.50005-7. URL: http://dx.doi.org/10.1016/B978-0-444-51958-0.50005-7 (cit. on p. 25).

[38] Bridgelux. *Bridgelux RS Array Series Product Data Sheet DS25 BXRA-xxx-3500-F, BXRA-xxx4000-H, BXRA-xxx7000-J, BXRA-40E4000-F, BXRA-40E4500-H, BXRA-40E7500-J, BXRA-xxC4500-F, BXRA-xxC5300-H, BXRA-xxC9000-J*. Tech. rep. URL: https://www.bridgelux.com/sites/default/files/resource{_}media/DS25-Bridgelux-RS-Array-Data-Sheet-2014.01.27.pdf (cit. on p. 25).

[39] Allen J Bard and Larry R. Faulkner. *Electrochemical Methods. Fundamentals and Fundamentals and Applications. 2nd Edition*. 2001. ISBN: 978-0-471-04372-0 (cit. on pp. 26, 27).

[40] A Cuesta, A Martınez-Alonso, and J.M.D Tascón. "Carbon reactivity in an oxygen plasma: a comparison with reactivity in molecular oxygen". In: *Carbon* 39.8 (2001), pp. 1135–1146. ISSN: 0008-6223. DOI: 10.1016/S0008-6223(00)00235-9. URL: https://www.sciencedirect.com/science/article/pii/S0008622300002359 (cit. on p. 34).

[41] Zafer Çiplak, Nuray Yildiz, and Ayla Cąlimli. "Investigation of graphene/Ag nanocomposites synthesis parameters for two different synthesis methods". In: *Fullerenes Nanotubes and Carbon Nanostructures* 23.4 (2015), pp. 361–370. ISSN: 15364046. DOI: 10.1080/1536383X.2014.894025. URL: http://www.tandfonline.com/doi/abs/10.1080/1536383X.2014.894025 (cit. on p. 42).

Part II

Budget

Chapter 6

Budget

In order to calculate the budget the following considerations were taken:

- All the equipment used in this research was already purchased and its cost is not exclusive of it, so the amortization was taken as a cost of this research. In order to calculate the amortization, the lifespan of the equipment is considered to be 10 years, being each year 200 laboral days.
- Some characterization techniques are offered as a service by the university/research centre with the next costs:
  - Atomic force microscopy: 13 € per hour per hour of service.
  - Raman spectroscopy: 10 € per hour of service.
  - X-ray photoelectron spectroscopy: 25 € per hour of service.

6.1 Budget break down

6.1.1 Synthesis of G-mat films

In this chapter, the synthesis of G-mat films is broken down in six sub-chapters.

Substrate preparation

This sub-chapter shows the budget for the preparation of the substrate. A 3000 € sonicator was used for a day.

Table 6.1: Substrate preparation budget.

6.1.1.1	Substrate preparation			
Amount	**Unit**	**Concept**	**Cost per unit (€)**	**Cost (€)**
7	ea.	Quartz substrate	10.00	70.00
0.2	L	Ultrapure water	0.51	0.10
0.2	L	Ethanol	15.00	3.00
0.2	L	Acetone	13.00	2.60
1	day	Sonicator	1.50	1.50
			Total	**77.20**

Precursor preparation

This sub-chapter shows the budget for the preparation of the substrate. A 800 € magnetic stirrer was used for a day.

Table 6.2: Precursor preparation budget.

6.1.1.2	Precursor preparation			
Amount	**Unit**	**Concept**	**Cost per unit (€)**	**Cost (€)**
2.4	g	Alginic acid from brown algae	0.43	1.03
3	mL	Ammonia solution 25%	0.02	0.06
0.03	L	Ultrapure water	0.51	0.02
1	day	Magnetic stirrer	0.40	0.40
12	ea.	45μ M regenerated cellulose syringe filters	0.50	6.00
			Total	**7.51**

Coating of quartz with the precursor

This sub-chapter shows the budget for the coating of the substrate with the precursor. A 1 000 € spincoater was used for a day.

Table 6.3: Coating of quartz with the precursor budget.

6.1.1.3	Coating of quartz with the precursor			
Amount	**Unit**	**Concept**	**Cost per unit (€)**	**Cost (€)**
1	day	POLOS spincoater	0.50	0.50
1	ea.	Pasteur pipette	0.05	0.05
			Total	**0.55**

Pyrolisis of the precursor films

This sub-chapter shows the budget for the pyrolysis of the precursor coated substrate. A 16000 € tube furnace was used for two days.

Table 6.4: Pyrolisis of the precursor films budget.

6.1.1.4 Pyrolisis of the precursor films

Amount	Unit	Concept	Cost per unit (€)	Cost (€)
2	day	Tube furnace	8.00	16.00
216	NL	Argon	0.05	10.80
			Total	**26.80**

Oxygen plasma treatment of ml-G

This sub-chapter shows the budget for the oxygen plasma treatment of the ml-G films. A 7 500 € plasma cleaner was used for a day.

Table 6.5: Oxygen plasma treatment of ml-G budget

6.1.1.5 Oxygen plasma treatment of ml-G

Amount	Unit	Concept	Cost per unit (€)	Cost (€)
1	day	Diener Femto plasma cleaner	3.75	3.75
50	NL	Oxygen	0.03	1.50
			Total	**5.25**

Photoelectrode preparation

This sub-chapter shows the budget for the preparation of the photoelectrodes.

Table 6.6: Photoelectrode preparation budget.

6.1.1.6 Photoelectrode preparation

Amount	Unit	Concept	Cost per unit (€)	Cost (€)
1	ea	Silver paint	30.00	30.00
1	ea	Polymeric paint	20.00	20.00
2	g	Paraloid B-72	0.02	0.04
0.07	L	Acetone	13.00	0.91
			Total	**50.95**

Overall cost of the chapter

In table 6.7 are collected the different sub-chapters showing the overall cost of the synthesis of the G-mat films.

Table 6.7: Synthesis of G-mat films budget.

6.1.1	**Synthesis of G-mat films**	
Chapter	**Concept**	**Cost (€)**
6.1.1.1	Substrate preparation	77.20
6.1.1.2	Precursor preparation	7.51
6.1.1.3	Coating of quartz with the precursor	0.55
6.1.1.4	Pyrolisis of the precursor films	26.80
6.1.1.5	Oxygen plasma treatment of ml-G	5.25
6.1.1.6	Photoelectrode preparation	50.95
	Total	**168.26**

6.1.2 Characterization

This chapter shows the budget for the characterization of the G-mat films.

Characterization services

This sub-chapter shows the budget for the characterization services. Atomic force microscopy requires 10 minutes for preparing the sample and 50 minutes to perform the scanning. A total of 1 hour per sample is needed and 4 samples were scanned. Raman microscopy requires 10 minutes per mapping. 3 mappings were made in each sample and 4 sample were measured. 2 hours of Raman spectroscopy serviced was required. X-ray photoelectron spectroscopy requires 1 hour of high vacuum before performing the scan and a 30 minute scan. A total of 4 samples were scanned.

Table 6.8: Characterization services budget.

6.1.2.1		**Characterization services**		
Amount	**Unit**	**Concept**	**Cost per unit (€)**	**Cost (€)**
4	h	Atomic force microscopy service	13.00	52.00
2	h	Raman spectroscopy service	10.00	20.00
6	h	X-ray photoelectron spectroscopy service	25.00	150.00
			Total	**222.00**

Characterization equipment

This sub-chapter shows the budget for the characterization equipment.

Table 6.9: Characterization equipment budget.

6.1.2.2	**Characterization equipment**			
Amount	**Unit**	**Concept**	**Cost per unit (€)**	**Cost (€)**
1	day	Keithley 2450 sourcemeter	3.00	3.00
1	ea.	Four-point collinear probe	50.00	50.00
1	day	Cary 50 Conc UV-Visible spectrophotometer	2.25	2.25
			Total	**55.25**

Overall cost of the chapter

In table 6.10 are collected the different sub-chapters showing the overall cost of characterization.

Table 6.10: Characterization budget.

6.1.2	**Characterization**	
Chapter	**Concept**	**Cost (€)**
6.1.2.1	Characterization services	222.00
6.1.2.2	Characterization equipment	55.25
	Total	**277.25**

6.1.3 Water splitting reaction tests

This chapter shows the budget for the photoelectrochemical tests.

Water splitting reaction tests

This sub-chapter shows the budget for the photoelectrochemical tests break down. A 8 000 € potentiostat/galvanostat was used during 7 days. A 600 € Electrochemical reactor was used for 7 days. A 50 000 € gas chromatograph was used during half day.

Table 6.11: Water splitting reaction tests budget.

6.1.3.1	Water splitting reaction tests			
Amount	**Unit**	**Concept**	**Cost per unit (€)**	**Cost (€)**
7	day	VersaSTAT 3 Potentiostat/Galvanostat	4.00	28.00
7	day	Electrochemical reactor	0.30	2.10
1	ea.	Bridgelux RS LED Array BXRA-50C5300-H-00	30.00	30.00
0.50	L	Ultrapure water	0.51	0.26
53.62	g	Lithium perchlorate, 98%	0.35	18.66
1050	NL	Nitrogen	0.001	1.05
1	ea.	Ag/AgCl reference electrode	100.00	100.00
1	ea.	25 mm x 25 mm Platinum sheet	350.00	350.00
0.5	day	Gas chromatograph	25.00	12.50
			Total	**542.57**

Overall cost of the chapter

In table 6.12 are shown the overall costs of the chapter.

Table 6.12: Water splitting reaction tests budget.

6.1.3	Water splitting reaction tests	
Chapter	**Concept**	**Cost (€)**
6.1.3.1	Water splitting reaction tests	542.57
	Total	**542.57**

6.1.4 Workforce

This chapter shows the budget for the workforce.

Workforce

This sub-chapter shows the budget for the workforce. A chemical engineer worked for 300 hours (12 ECTS). The tutor dedicated 30 hours to oversee the different stages of the work.

Table 6.13: Workforce budget.

6.1.4.1	Workforce			
Amount	**Unit**	**Concept**	**Cost per unit (€)**	**Cost (€)**
300	h	Chemical engineer	30.00	9000.00
30	h	Tutor	42.00	1260.00
			Total	**10260.00**

Overall cost of the chapter

In table 6.14 are shown the overall costs of the chapter.

Table 6.14: Workforce budget.

6.1.4	**Workforce**	
Chapter	**Concept**	**Cost (€)**
6.1.4.1	Workforce	10260.00
	Total	**10260.00**

6.2 Total budget

In this section, the broken down budget is put together, table 6.15. General costs and taxes are added in order to obtain the overall budget of the research.

Table 6.15: Total budget

C	**Total budget**	
Chapter	**Concept**	**Cost (€)**
6.1.1	Synthesis of G-mat films	168.26
6.1.2	Characterization	277.25
6.1.3	Water splitting reaction tests	542.57
6.1.4	Workforce	10260.00
	Total	**11248.08**

The overall budget of the research ascends to 11248 EUROS AND 8 CENTS.

Table 6.16

TOTAL BUDGET	11248.08
General expenses (10%)	1124.81
TOTAL BEFORE TAXES	12372.89
21% Taxes	2598.31
TOTAL BUDGET AFTER TAXES	14971.19

The overall budget after taxes of the research ascends to 14971 EUROS AND 19 CENTS